Remote Sensing of Environment 211 (2018) 71–88

Contents lists available at ScienceDirect

Remote Sensing of Environment

journal homepage: www.elsevier.com/locate/rse

Long-term record of top-of-atmosphere albedo over land generated from AVHRR data

Zhen Song[a,b,c], Shunlin Liang[c,*], Dongdong Wang[c], Yuan Zhou[c], Aolin Jia[a,b]

[a] State Key Laboratory of Remote Sensing Science, Jointly Sponsored by Beijing Normal University and Institute of Remote Sensing and Digital Earth of Chinese Academy of Sciences, Beijing 100875, China

[b] Beijing Engineering Research Center for Global Land Remote Sensing Products, Institute of Remote Sensing Science and Engineering, Faculty of Geographical Science, Beijing Normal University, Beijing 100875, China

[c] Department of Geographical Sciences, University of Maryland, College Park, MD, 20742, USA

ARTICLE INFO

Keywords:
TOA albedo
AVHRR
CERES
CM SAF
Earth's energy budget
Climate change

ABSTRACT

Top-of-atmosphere (TOA) albedo is a fundamental component of Earth's energy budget. To date, long-term global land TOA albedo products with spatial resolution higher than 20-km are not available. In this study, we propose a novel algorithm to retrieve TOA albedo from multispectral imager observations acquired by Advanced Very High Resolution Radiometer (AVHRR), which provides the longest continuous record of global satellite observations since 1981. Direct estimation models were established first to derive instantaneous TOA broadband albedo under various atmospheric and surface conditions, including cloudy-sky, clear-sky (snow-free) and snow-cover conditions. To perform long-term series analysis, the instantaneous TOA albedo were then converted to daily/monthly mean values based on the diurnal curves from multi-year Clouds and the Earth's Radiant Energy System (CERES) 3-hourly flux dataset. Calibration differences between sequential AVHRR sensors were further mitigated by invariant targets normalization. The retrieved TOA albedo at 0.05° × 0.05° was validated against two TOA albedo datasets, CM SAF (Climate Monitoring Satellite Application Facility) flux data and CERES flux data, at spatial resolutions of 0.05° × 0.05°, 20 km × 20 km and 1° × 1°. The instantaneous TOA albedo had an overall Root-Mean-Square-Error (RMSE) of 0.047 when compared with 20-km CERES fluxes, whereas the 1° by 1° monthly mean TOA albedo showed closer agreements with both CM SAF and CERES, with RMSE ranging from 0.029 to 0.040 and from 0.022 to 0.031, respectively. Moreover, our product was found to be highly consistent with both CERES and CM SAF at long-term trend detection. The extensive validation indicated the robustness of our algorithm and subsequently, comparable data quality with existing datasets. With global coverage and long time series (1981–2017), our product is expected to provide valuable information for climate change studies.

1. Introduction

Top-of-atmosphere (TOA) albedo (also known as planetary albedo) is the fraction of the incoming solar flux reflected by Earth back into space. The variability of reflected energy influences our climate system by changing the Earth's energy budget (Palle et al., 2016; Stephens et al., 2015; Trenberth et al., 2009; Von Schuckmann et al., 2016). Since the TOA incoming solar flux is relatively constant, the reflected energy is mainly determined by TOA albedo. Therefore, TOA albedo is an important component in the climate system and Earth's radiation budget (ERB). The history of ERB measurements dates back to 1960s with the instruments on board the Explorer 6 and 7 satellites while the broadband instruments designed specifically for ERB monitoring started from the payloads of the Nimbus 6 and 7 satellites since 1975 (House et al., 1986; Jacobowitz et al., 1984). After Nimbus observations, the Earth Radiation Budget Experiment (ERBE) (Barkstrom, 1984; Jacobowitz et al., 1984), the Scanning Radiometer for Radiation Balance (ScaRaB) (Kandel et al., 1998), the Clouds and the Earth's Radiant Energy System (CERES) (Wielicki et al., 1996) and the Geostationary Earth Radiation Budget (GERB) (Harries et al., 2005) began operation in 1984, 1994, 1998 and 2002, respectively and these broadband measurements are vital radiation monitoring systems currently in use. The products from the broadband systems serve as irreplaceable data sources in the study of Earth's energy budget and climate change at the global scale (Dewitte and Clerbaux, 2017; Dewitte et al., 2013; Liang, 2017; Liang et al., 2010; Stephens et al., 2012; Trenberth et al., 2016; Wild, 2009; Wong et al., 2006).

There has been an increasing need for long-term, high-resolution

* Corresponding author at: Department of Geographical Sciences, University of Maryland, 2181 LeFrak Hall, College Park, MD 20742, USA.
E-mail address: sliang@umd.edu (S. Liang).

https://doi.org/10.1016/j.rse.2018.03.044
Received 17 October 2017; Received in revised form 27 March 2018; Accepted 31 March 2018
Available online 12 April 2018
0034-4257/ © 2018 Elsevier Inc. All rights reserved.

Table 1
Current available TOA albedo products from broadband sensors.

Dataset	Spatial resolution	Spatial coverage	Time span	Temporal resolution	Sensors	Website	References
ERBE	40 km at nadir*/2.5°	Global	1984–1990	Instantaneous*/daily/monthly	ERBE	https://eosweb.larc.nasa.gov/project/erbe/erbe_table	(Barkstrom, 1984; Jacobowitz et al., 1984)
CERES	20 km at nadir*/1°	Global	1997–1998; 2000–present	Instantaneous*/hourly/3-hourly/daily/monthly	CERES	https://ceres.larc.nasa.gov/order_data.php	(Loeb et al., 2018; Loeb et al., 2005; Loeb et al., 2002; Wielicki et al., 1996)
GERB	50 km at nadir*/50 km	European	2002–present	Instantaneous*/15 min	GERB	http://ggsps.rl.ac.uk/	(Harries et al., 2005)
ScaRaB	40 km at nadir*/1°	30°S–30°N	1994–1995; 1998–1999; 2011–present	Instantaneous*/1–7 times daily	ScaRaB	http://www.icare.univ-lille1.fr/mt/products	(Duvel et al., 2001; Kandel et al., 1998; Roca et al., 2015)

* The asterisked spatial resolutions corresponded to the products with asterisked temporal resolutions.

TOA albedo products in monitoring the climate impacts of regional-scale events, such as air pollution, urbanization, forest fires, and other small-scale land cover changes (Chen and Loboda, 2018; Song et al., 2017; Zhang et al., 2015) while the broadband sensors are basically limited to the coarse resolutions: high-level CERES products provide 1-degree resolution, the ERBE data is approximately 250 km, and GERB data is 50 km at nadir (details shown in Table 1). Therefore, to meet the needs of regional energy balance and climate change applications, several studies have attempted to retrieve the high spatial resolution TOA albedo based on multispectral narrowband sensors. Wang and Liang (2016) proposed a direct estimation method based on radiative transfer simulations and applied this method to Moderate Resolution Imaging Spectroradiometer (MODIS) data. The TOA Albedo based on MODIS (hereafter TAL-MODIS) showed good agreement with CERES products and had a high spatial resolution of 1 km. Using Spinning Enhanced Visible Infrared Imager (SEVIRI) data, Niu and Pinker (2012) transformed the TOA narrowband apparent reflectance to broadband reflectance and then applied a newly developed Angular Distribution Model (ADM) to estimate the TOA albedo. However, due to the temporal limitations of the source data, the algorithms based on MODIS and SEVIRI could only provide data starting from the year 2000. By involving Meteosat observations, a recently released long-term high spatial resolution (0.05° by 0.05°) products from Climate Monitoring Satellite Application Facility (CM SAF), formed by European Organisation for the Exploitation of Meteorological Satellites (EUMETSAT), provided TOA albedo from 1983 to 2015 but their spatial coverage was limited to 70° N–70° S, 70° W–70° E (Urbain et al., 2017a). The Advanced Very High Resolution Radiometer (AVHRR) aboard National Oceanic and Atmospheric Administration (NOAA) polar-orbiting satellites provides Global Area Coverage (GAC) data at 4-km resolution. The earliest AVHRR sensor was carried on TIROS-N in 1978, followed by NOAA-6 and to the most recent satellite, NOAA-19. Thus, the AVHRR data constitute the longest global satellite observation record. The AVHRR Polar Pathfinder Project and the Extended AVHRR Polar Pathfinder Project (App and App-x) (Key et al., 2001; Wang and Key, 2005a, 2005b) had utilized AVHRR data, but only provided TOA albedo over the Polar Regions. There are also some long-term time series surface albedo datasets based on AVHRR data (Liu et al., 2013; Riihelä et al., 2013; Sütterlin et al., 2015). However, to date, long-term high spatial resolution TOA albedo products with global coverage over land are not publically available (details shown in Table 2).

Typical approach for estimating the broadband albedo from narrowband radiation includes two steps: first, anisotropic correction from directional reflectance to semi-hemispherical albedo is applied, usually by ADM built by multi-angle observations; and second, narrowband-to-broadband albedo conversion is conducted. The reflected radiation at TOA is the sum of incoming solar energy reflected by both surface and atmosphere and therefore is both surface- and atmosphere- dependent. The typical TOA ADM is normally divided by different scene types for specific surface and atmospheric combination (Hucek and Jacobowitz, 1995; Loeb et al., 2003; Suttles et al., 1988). For the sensors onboard the solar-orbiting satellites, like MODIS and AVHRR, it is hard to collect multi-angle observations within a short period for a specific scene type. Instead, observations from multi-days were obtained and used for the ADM building (Hucek and Jacobowitz, 1995; Loeb et al., 2005). However, during the collecting days the scene type may have changed and the inconsistent scene type would lead to errors in ADM. Moreover, the two-step method may lead to the accumulation and propagation of errors from the anisotropic correction and narrowband-to-broadband conversion to the final results.

In this study, instead of building the ADM dependent on scene type classification, we develop models utilizing spectral information to correct the anisotropic impact. The essence of this method is to estimate albedo from spectral information by establishing the relationship between TOA multispectral reflectance and TOA albedo at a specific solar/viewing geometry. The independent variable of the model is the

Table 2
Current available TOA albedo products from narrowband sensors.

Dataset	Spatial resolution	Spatial coverage	Time span	Temporal resolution	Sensors	Website	References
APP	5 km	Arctic/Antarctic	1982–present	Twice-daily	AVHRR	https://www.ncdc.noaa.gov/cdr/fundamental/avhrr-polar-pathfinder-app	(Key et al., 2001)
APP-x	25 km	Arctic/Antarctic	1982–present	Twice-daily	AVHRR	https://www.ncdc.noaa.gov/cdr/atmospheric/extended-avhrr-polar-pathfinder-app-x	(Wang and Key, 2005a, 2005b)
TAL-MODIS	1 km	Global	2000–present	Instantaneous/daily	MODIS	To be released	(Wang and Liang, 2016, 2017)
MISR	35.2 km	Global	2000–present	Daily/monthly	MISR	https://eosweb.larc.nasa.gov/project/misr/version/pge8c	(Diner et al., 1999)
CM SAF	0.05 degree	70°N–70°S, 70°W–70°E	1983–2015	Daily/monthly	MVIRI/SEVIRI	http://www.cmsaf.eu/EN/Data_Access/Data_Access_node.html	(Urbain et al., 2017a)
TAL-AVHRR	0.05 degree	Global	1981–present	Instantaneous/daily/monthly	AVHRR	http://www.geodata.cn/ http://glcf.umd.edu/data	This study

multispectral reflectance at the specific solar/viewing angle. Furthermore, to mitigate the accumulated errors by multi-processing steps, we directly link the narrowband reflectance to broadband albedo. This direct estimation method has been successfully applied in surface and TOA albedo retrieval (He et al., 2015; Liang et al., 2005; Qu et al., 2014; Tang et al., 2006; Wang and Liang, 2016). The satellite observations were assumed to be more accurate than modeled fluxes by radiative transfer simulations, therefore, we extracted the training data pairs from the coincident AVHRR data and MODIS TOA albedo, retrieved by Wang and Liang (2016) by direct estimation method, for model development. Applying this direct estimation model, the instantaneous TOA albedo at the specific time of the day was retrieved from AVHRR observations. However, in the studies of Earth's energy budget, the daily/monthly mean TOA albedo, which is the integration of all the instantaneous values in a given day/month, is of greater significance (Doelling et al., 2013; Wang and Liang, 2017). For AVHRR data, the orbit drift is also a concern and the observation time at a specific location varies from day to day, making it even difficult to conduct the long-term analysis based on these instantaneous data. Thus, converting the instantaneous TOA albedo to daily/monthly mean TOA albedo was also necessary before applying these datasets in long-term analysis.

Therefore, the goal of this study is to develop a new method to retrieve a complete record of daily/monthly mean TOA albedo from AVHRR data since 1981, supporting the studies of climate models and climate change. The TOA ALbedo based on AVHRR was name as TAL-AVHRR hereafter. Section 2 of this paper provides a brief introduction of the data, methods are described in Section 3, and Section 4 presents the algorithm performance and the validation results. Uncertainties are analyzed in Section 5. A summary and ideas for future work are discussed in Section 6.

2. Data

2.1. AVHRR

The AVHRR TOA reflectance data used (AVH02C1) in this study were obtained from Version 4 of the land Long-Term Data Record (LTDR, http://ltdr.nascom.nasa.gov/) project. The project provided a consistent AVHRR dataset at a spatial resolution of 0.05°, from 1981 to the present (Pedelty et al., 2007), based on GAC data from the AVHRR sensors, and the best available data was selected if multiple observations were available in a day. AVHRR observations provided spectral bands at visible channel (0.580–0.680 μm), near-infrared channel (0.725–1.100 μm) and thermal channels and both the visible and near-infrared channel in the shortwave range were used in our TOA albedo retrieval. However, due to the lack of on-board calibration systems for the visible and near-infrared channels, the AVHRR source data needs to be carefully calibrated first. LTDR applied the invariant target calibration based on radiative transfer model (Franch et al., 2017; Vermote and Kaufman, 1995; Vermote and Saleous, 2006) and demonstrated a calibration accuracy within 1% compared to MODIS (Vermote and Saleous, 2006). The calibration was followed by several steps. First, spectral and directional characteristics were collected for invariant targets based on multi-year MODIS data. Then, the top-of-atmosphere radiance of these invariant targets was calculated by radiative transfer model at AVHRR channels, with inputs of the atmospheric parameters obtained from assimilated data and the kernel-driven bidirectional reflectance distribution function (BRDF) models collected in the first step. Finally, the calibration coefficients were generated from the observed AVHRR radiance and the computed radiance. Moreover, LTDR employed a clock correction approach (Evans et al., 2010) for geolocation correction and the results achieved an geolocation accuracy better than two pixels.

The Version 4 LTDR also provided an improved cloud mask compared to previous versions, which matched well with the MODIS cloud

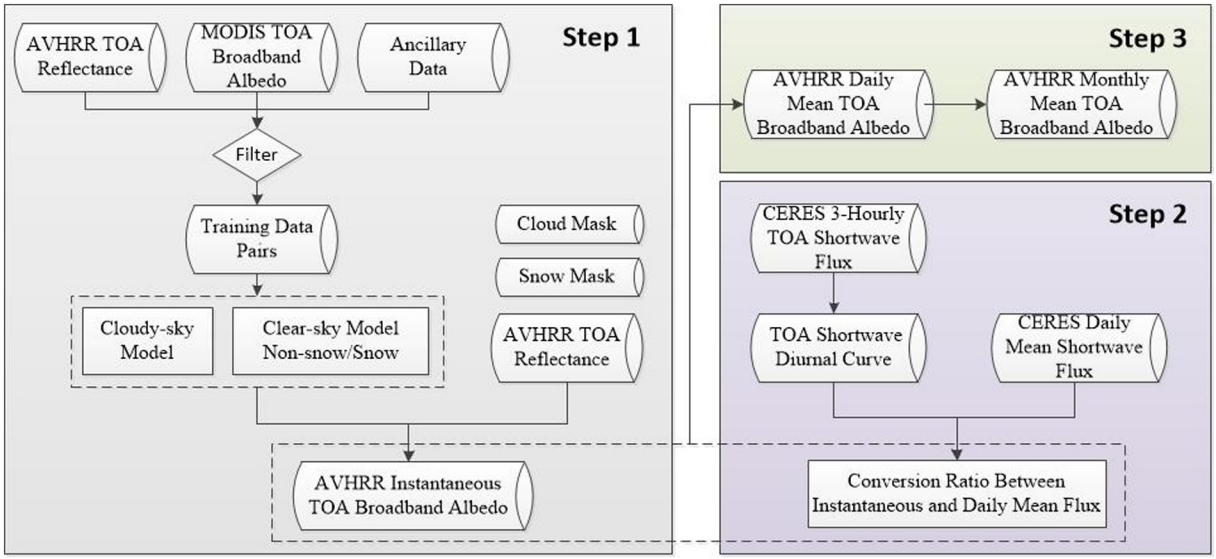

Fig. 1. Flowchart of TOA broadband albedo estimation from AVHRR data.

mask at a consistency > 90% (Franch et al., 2017). AVHRR snow cover data was obtained from Japan Aerospace Exploration Agency (JAXA) Satellite Monitoring for Environmental Studies (JASMES) (Hori et al., 2017). The overall accuracy of JASMES snow cover is over 0.82 for all seasons compared to in-situ measurements.

2.2. MODIS

MODIS instruments are onboard Terra and Aqua polar-orbiting satellites and have 36 spectral bands with resolutions from 250 m to 1 km. A 1-km high-spatial-resolution TOA albedo dataset based on MODIS data was recently generated by Wang and Liang (2016). A hybrid algorithm was built to estimate TOA albedo directly from TOA spectral reflectance, based on extensive radiative transfer simulations. These simulations were constituted by representative surface and atmospheric combinations and accounted for both the surface and atmospheric anisotropic properties. The surface BRDF were calculated from Polarization and Directionality of the Earth's Reflectances (POLDER) radiometer based on kernel-driven models and the atmospheric characteristics were generated by Modtran 5. Representative aerosol types, aerosol optical depth loadings, water-vapor concentrations were considered in the clear-sky conditions while a wide range of cloud types, cloud base height, cloud optical depth and water-vapor concentrations were involved in the cloudy-sky conditions. Based on the extensive simulations, clear sky model and cloudy sky model were developed separately and a model over snow-cover condition was built specifically. The retrieved instantaneous TAL-MODIS demonstrated good agreement with the CERES TOA flux products, with a RMSE of 0.036 for Terra and 0.039 for Aqua at CERES footprint resolution (~20 km). Due to its good agreement with CERES and high spatial resolution, we take TAL-MODIS as training data in our study. In addition, auxiliary datasets including cloud mask products (MYD35_L2 C6) and snow cover data (MYD10C1 C6) were also used in the training process. To keep time consistency with AVHRR, we only use data from the afternoon satellite Aqua.

2.3. CERES

CERES is a broadband instrument measuring shortwave reflected radiation (0.3–5 μm), longwave Earth-emitted thermal radiation (8–12 μm) and all wavelengths of radiation (0.3–200 μm), onboard Terra, Aqua and Suomi NPP, with 20-km spatial resolution at nadir. CERES fluxes were regarded as the most accurate products at a coarse resolution and therefore were used as our main references for the validation. CERES shortwave fluxes were generated by ADM based on the observed shortwave radiance (Loeb et al., 2005). The Level-2 Single Scanner Footprint (SSF) products provided instantaneous TOA albedo at a resolution of 20 km and CERES Level-3 Synoptic products (SYN1deg) provided 3-hourly and daily/monthly mean TOA radiative fluxes since 2000 (Doelling et al., 2013). The 3-hourly shortwave fluxes had incorporated the real-time cloud and aerosols properties from both MODIS and geostationary satellite, taking account the diurnal variations of atmospheric conditions. Thus, our study utilized CERES 3-hourly shortwave fluxes to build the relationship between instantaneous fluxes and the daily mean ones. Our retrieved instantaneous and monthly mean TOA albedo were then compared with the CERES SSF and SYN data respectively. The CERES Energy Balanced and Filled (EBAF) data was also used to further validate our datasets at revealing the long-time scale climate trends. All the products from CERES were from the latest edition 4A.

2.4. CM SAF

The Climate Monitoring Satellite Application Facility (CM SAF) have just released a data record of TOA radiation with the first version (TOA_MET_V001) in 2017 (Urbain et al., 2017b), based on Meteosat MVIRI and SEVIRI instruments. An empirical narrowband to broadband conversion models and CERES ADM models were used to compute the broadband fluxes (Urbain et al., 2017a). This dataset covers the region 70°N–70°S and 70°W–70°E at a spatial resolution of 0.05° since 1983. We use this dataset as a cross-validation reference due to the same spatial resolution with our products as well as its long-term series coverage.

3. Methodology

Our objective is to retrieve the long-term TOA broadband albedo from AVHRR TOA reflectance. The framework is composed of three steps (Fig. 1). In the first step, extensive training data pairs were obtained from coincident AVHRR and MODIS observations. The direct estimation algorithm was then developed based on the data pairs, retrieving instantaneous TOA broadband albedo directly from AVHRR TOA reflectance. Second, the instantaneous TOA albedo was converted to daily mean TOA albedo according to the diurnal curve captured by CERES 3-hourly flux data. Finally, the daily mean TOA albedo was integrated to the monthly mean TOA broadband albedo.

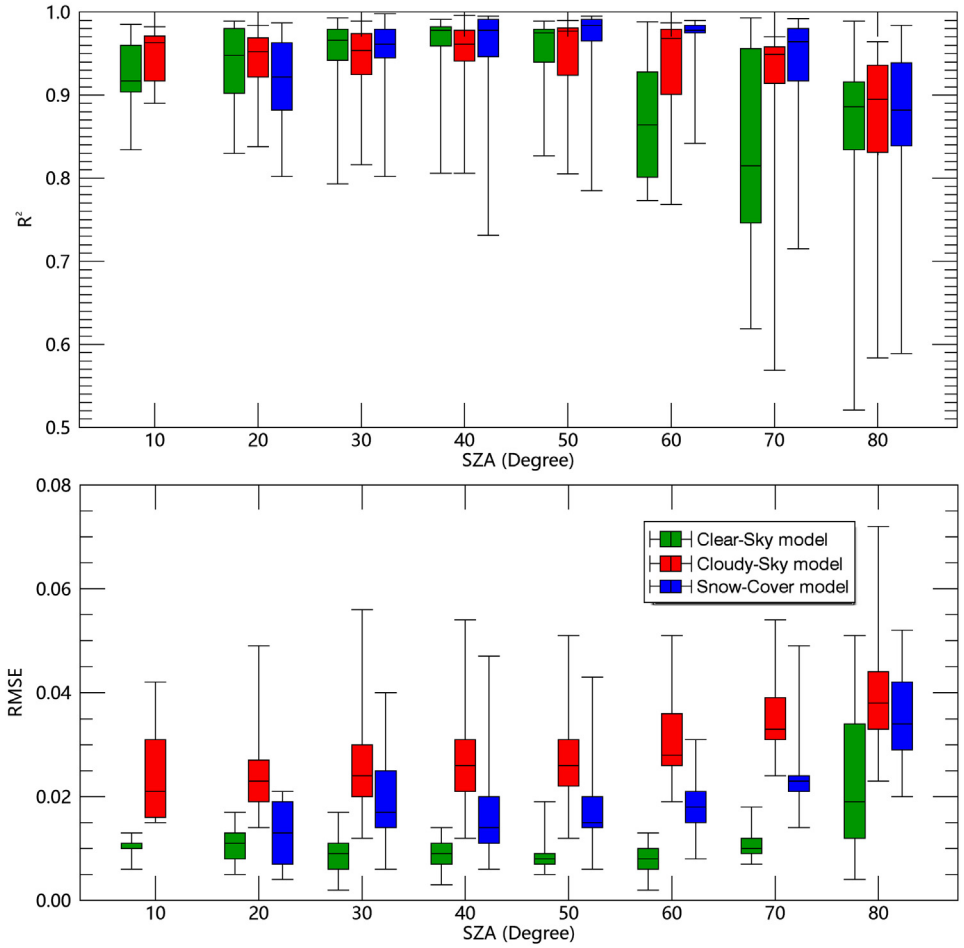

Fig. 2. Fitting accuracy for the clear-sky model, cloudy-sky model and snow-cover model. The statistics (R^2, RMSE) were grouped by SZA. For each box, the middle line, upper hinges and lower hinges represent the R^2 (RMSE) median, 25th (75th) percentile, and 75th (25th) percentile, respectively. The whiskers extend to the largest R^2 (RMSE) and the smallest R^2 (RMSE).

3.1. Direct estimation algorithm for instantaneous TOA broadband albedo

The basic idea of the direct estimation method is to establish the direct statistical relationship between narrowband TOA reflectance and broadband TOA albedo, instead of passing through the two steps of transforming the narrowband reflectance to narrowband albedo and converting the narrowband albedo to broadband albedo. In this study, the training data for the model building was collected from real AVHRR observations and high-resolution TOA albedo datasets retrieved from MODIS (Wang and Liang, 2016); the MODIS TOA values were taken as the "true values" in the training process. In addition, due to the directional characteristics of the TOA radiance distribution, our training dataset was stratified by different solar/viewing geometries (including the solar zenith angle (SZA) θs, satellite view zenith angle (VZA) θv and relative azimuth angle (RAA) φ). Consequently, Eq. (1) gives the estimation model of the instantaneous TOA albedo:

$$\alpha_{sw} = f_{\theta_s,\theta_v,\varphi}(\rho_{toa}) \quad (1)$$

where α_{sw} is the TOA broadband albedo from MODIS, f is the linear regression model under different solar/viewing geometries, and ρ_{toa} is the AVHRR TOA reflectance including the visible band (0.580–0.680 μm) and near-infrared band (0.725–1.100 μm). We stratified SZA at 0°, 10°, 20°, 30°, 40°, 50°, 60°, 65°, 70°, 75°, 80°, 85° and 90°; VZA at 0°, 10°, 20°, 30°, 40°, 50°, 60°, 65°, 70° and 75°; and RAA at 0°, 30°, 60°, 90°, 120°, 150°, and 180°. Model coefficients in f are stored as a look-up-table (LUT) dependent on solar/viewing geometry.

To obtain representative training data pairs (ρ_{toa}, α_{sw}) for different combinations of surface and atmospheric conditions, we had collected four months of global collocated AVHRR and MODIS data from different seasons in 2007. A total of 28,144,761 data pairs was collected, covering 16 IGBP surface types and a wide range of atmospheric conditions from different seasons and climatic zones. In practice, MODIS instantaneous TOA albedo (swath data) were first projected to global maps at 0.05-degree scale, matching the spatial resolution of AVHRR. For the multi-observations over high latitude region, the closest observation to the corresponding AVHRR pixel was selected and stored. Because our model is built based on pixel-to-pixel samples, the geolocation accuracy is of significance to obtain reliable training samples. To mitigate the possible geolocation error (2–3 pixel shift at the poorest-geolocation pixel) between AVHRR and MODIS as well as the possible shifts of the advective clouds in the sampling time window (Bhatt et al., 2016; Wielicki et al., 2008), we aggregated both datasets by a 5 × 5 pixel moving window before matching them to the training data pairs. To keep more samples and more dynamics in the source data, we use rotating aggregation windows by every 0.05-degree step instead of a regular 5 × 5 resampling. Except for the TOA broadband albedo, the cloud fraction from MODIS cloud products, snow fraction from MODIS snow products, observation time and solar/view geometries were also recorded.

Based on the gridded MODIS datasets, training data pairs were then selected from coincident AVHRR and MODIS observations. We assumed that the surface and atmospheric conditions remained unchanged in 5 min and limited the acquisition time of the two datasets within 5 min. In addition, TOA albedo is a function of SZA (Loeb et al., 2005; Wang

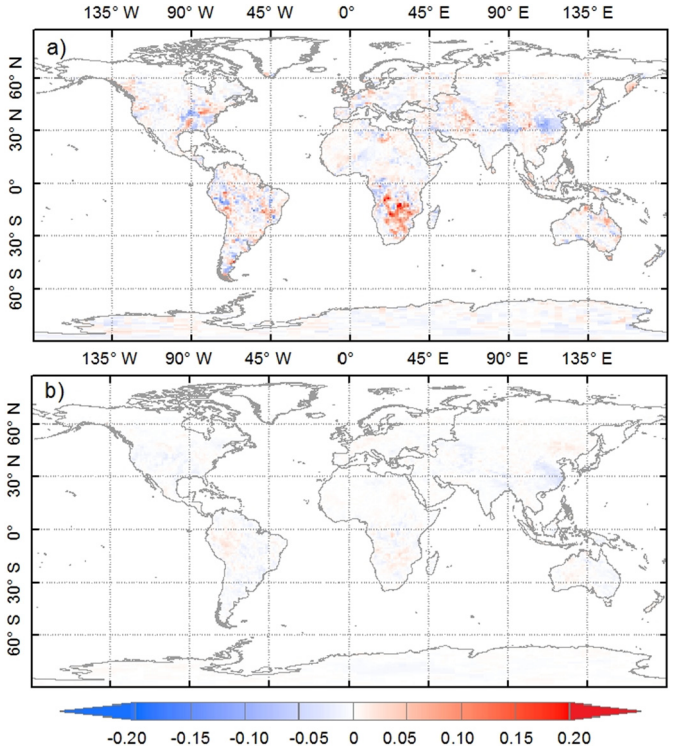

Fig. 3. TOA albedo differences between the result from real-time conversion ratio and the one from climatology conversion ratio for a) daily mean TOA albedo in January, 10, 2008 and b) monthly mean TOA albedo in January 2008.

et al., 2005) and normally has a larger value at high SZA. To extract the exact TOA albedo for the AVHRR observations, we further controlled the consistency of SZA of the two datasets.

We built separate models for clear-sky and cloudy-sky conditions. The clear-sky condition was defined as no cloud coverage while all the other conditions with cloud fractions > 0 were defined as cloudy-sky condition. As we had limited the time difference between AVHRR and MODIS observations to 5 min, we could assume that the cloud conditions didn't change between the selected data pairs. MODIS cloud mask was reported to have high accuracy (Ackerman et al., 2008) and therefore was used here to screen the clear-sky or cloudy-sky samples. Further, for clear-sky condition, snow-covered surface was modeled separately from non-snow surface due to the unique BRDF characteristics and the snow-covered pixels were selected by high-accuracy MODIS snow product(Hall and Riggs, 2007). Finally, we had cloudy-sky models for cloudy-sky conditions, clear-sky models for clear-sky snow-free regions and snow-cover models for snow-covered conditions. In the retrieval procedure, the AVHRR cloud mask and snow mask were taken as the input data to apply the specific model to the corresponding condition.

3.2. Conversion from instantaneous to daily mean TOA albedo

Daily mean TOA albedo is the ratio between daily mean shortwave upward flux and the shortwave downward flux at the top of the atmosphere, which can be expressed as,

$$\alpha_{daily} = \frac{F_{sw-up}^{daily}}{F_{sw-down}^{daily}} \quad (2)$$

where $F_{sw-down}^{daily}$ is the daily mean shortwave downward flux, the mean of all the instantaneous downward flux during the day, which is determined by the sun–earth distance and solar zenith angle. Therefore, at a given location for a specific day of the year, $F_{sw-down}^{daily}$ is a constant. F_{sw-up}^{daily} is the daily mean shortwave upward flux, the mean of all the instantaneous shortwave upward flux (F_{sw-up}^{instan}) during the entire day. F_{sw-up}^{instan} has a diurnal cycle and is determined by the diurnal variations of solar zenith angle and changes of atmospheric conditions (Rutan et al., 2014; Taylor, 2014a; Taylor, 2014b; Taylor and Loeb, 2013). Based on the CERES 3-hourly flux data and daily flux data, a look-up-table of conversion ratios between F_{sw-up}^{daily} and F_{sw-up}^{instan} were constructed; this look-up-table combines the influences from solar zenith angle and atmospheric conditions by employing geostationary data. The conversion is expressed by,

$$F_{sw-up}^{daily} = r * F_{sw-up}^{instan}(t) \quad (3)$$

where r is the ratio between F_{sw-up}^{daily} and F_{sw-up}^{instan}, and is dependent on the observation time, the location and the day of the year. The conversion ratio LUTs were built every three hours in a day and for an observation time *t*, we got the corresponding conversion ratio by the linear interpolations of the nearby 3-hour ratios. $F_{sw-up}^{instan}(t)$ is determined by the instantaneous TOA albedo and instantaneous TOA shortwave downward flux with the following expression,

$$F_{sw-up}^{instan} = \alpha_{instan} * F_{sw-down}^{instan} \quad (4)$$

With α_{instan} retrieved from Section 3.1 and a constant $F_{sw-down}^{instan}$ for a specific location/time, F_{sw-up}^{instan} is calculated by Eq. (4). Then, based on the conversion ratio LUTs, F_{sw-up}^{instan} is converted to the daily mean shortwave upward flux F_{sw-up}^{daily} by Eq. (3). Finally, the daily mean TOA albedo is calculated as the ratio of the daily mean shortwave upward flux F_{sw-up}^{daily} and daily mean shortwave downward flux $F_{sw-down}^{daily}$.

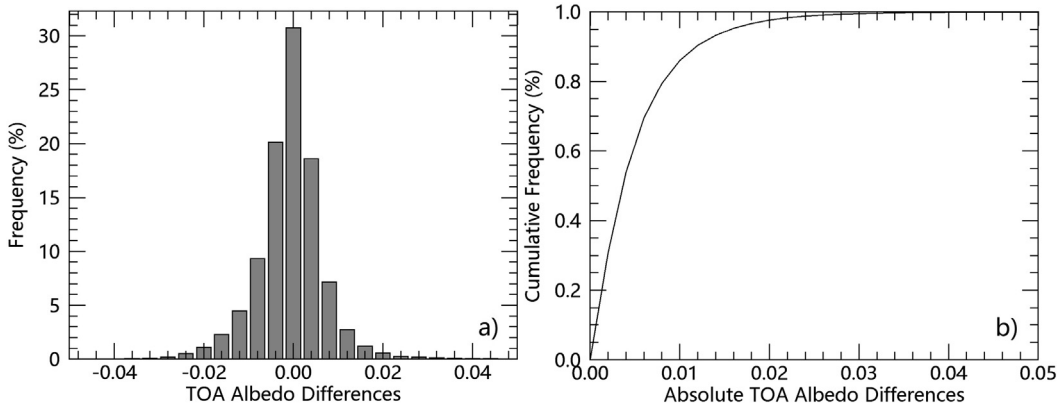

Fig. 4. Distribution of monthly mean TOA albedo differences between the results from real-time conversion ratio and climatology conversion ratio for 12 months in 2008 for a) TOA albedo differences (real-time minus climatology) and b) Absolute value of TOA albedo differences.

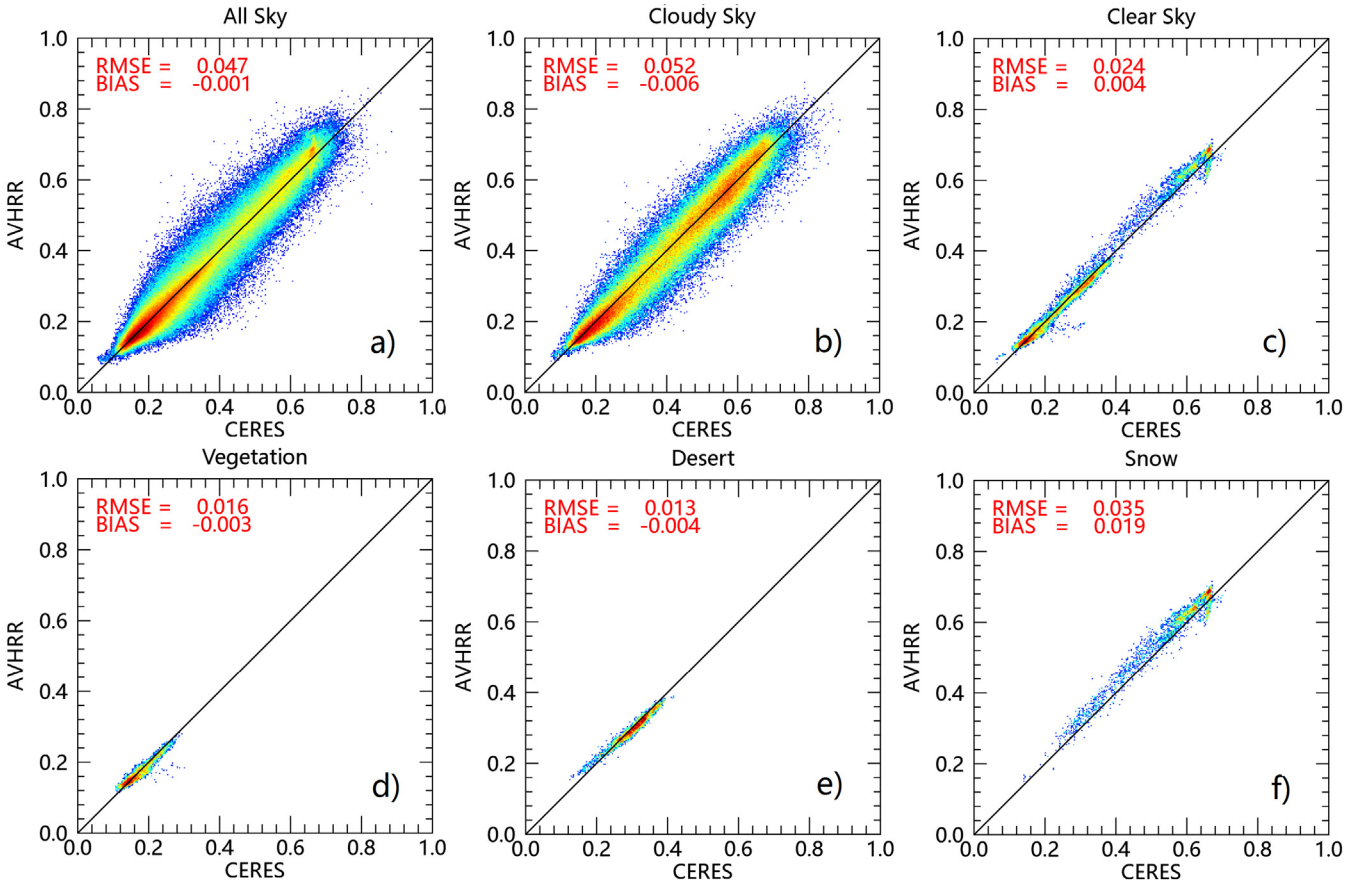

Fig. 5. Instantaneous TAL-AVHRR comparison with CERES at 20 km × 20 km footprint at different atmospheric conditions for twelve days in 2008 (one day for each month) a) all sky b) cloudy sky c) clear sky and different land cover types d) vegetation e) desert and f) snow. Only the samples with consistent CERES and AVHRR cloud fraction were chosen in the comparisons under cloudy sky (b) and clear sky (c,d,e,f) for the model evaluation.

3.3. Long term daily/monthly mean TOA albedo generation

Building the conversion ratio between F_{sw-up}^{daily} and F_{sw-up}^{instan} is the key for the daily mean TOA albedo calculation. For the years after 2000, the conversion ratio could be calculated from the real-time CERES flux products for the diurnal variation correction (hereinafter real-time conversion ratio). However, this real-time conversion ratio could not be applied for years before 2000, when CERES data were not available. Here, based on multi-year CERES flux data from 2003 to 2014, a climatology conversion ratio was built for the long-term daily mean TOA albedo estimation. A previous study suggested that the diurnal variability of TOA albedo can be largely explained by its dependence on SZA(Rutan et al., 2014). And the solar zenith angle is determined by the observation time, the location and the day of the year. Thus, based on the multi-year diurnal cycles, linear regression models were built to predict the daily mean flux from the instantaneous flux, depending on the observation time, the location and the day of the year. The linear regression model is expressed by:

$$F_{sw-up}^{daily} = r * F_{sw-up}^{instan}(t) + b \quad (5)$$

where r is the scale factor from F_{sw-up}^{instan} to F_{sw-up}^{daily}, and b is the offset of the regression model. We found that all of the models had offset b < 0.0001 (b = 0 for 93% models). Thus, Eq. (5) had almost the same expression as Eq. (3). Once we have F_{sw-up}^{daily}, the method to calculate the TOA albedo is just as described in Section 3.2. To keep data consistency, we rely on the climatology conversion ratio to calculate the daily mean TOA albedo for the entire time series from 1981 to present. From daily mean to monthly mean values, the monthly mean upward shortwave flux was first calculated from the average value of the daily mean upward shortwave flux. Monthly mean TOA albedo can then be derived as the ratio of the monthly mean reflected shortwave flux and monthly mean incident solar flux at the top of the atmosphere.

4. Results

4.1. Algorithm performance

4.1.1. Fitting accuracy of the models for instantaneous TOA albedo

As described in Section 3.1, thousands of data pairs were used to build the models for instantaneous TOA albedo estimation. The clear-sky model and cloudy-sky model were developed separately for clear sky conditions (snow-free) and cloudy sky conditions, respectively, while the snow-cover model was built explicitly for the snow covered region. All of the models were dependent on the view geometry defined by SZA, VZA and RAA. Due to the strong relationship between TOA albedo and SZA, we divided all the angular dependent models by SZA and Fig. 2 shows the statistics (R-Square, R^2 and Root Mean Square Error, RMSE) of model fitting accuracy by the SZA groups. For each SZA group, different VZA bins (0°, 10°, 20°, 30°, 40°, 50°, 60°, 65°, 70° and 75°) and RAA bins (0°, 30°, 60°, 90°, 120°, 150° and 180°) were included.

In general, clear-sky models, cloudy-sky models and snow-cover models all showed better fitting accuracy at smaller SZA. When SZA was < 70°, R^2 of the models varied from 0.73 to 0.99 and RMSE ranged from 0.004 to 0.056. Among them, 75% of the models had fitting results with R^2 > 0.9 and RMSE < 0.030. Three types of models showed similar fitting accuracy in terms of R^2 while RMSE displayed different

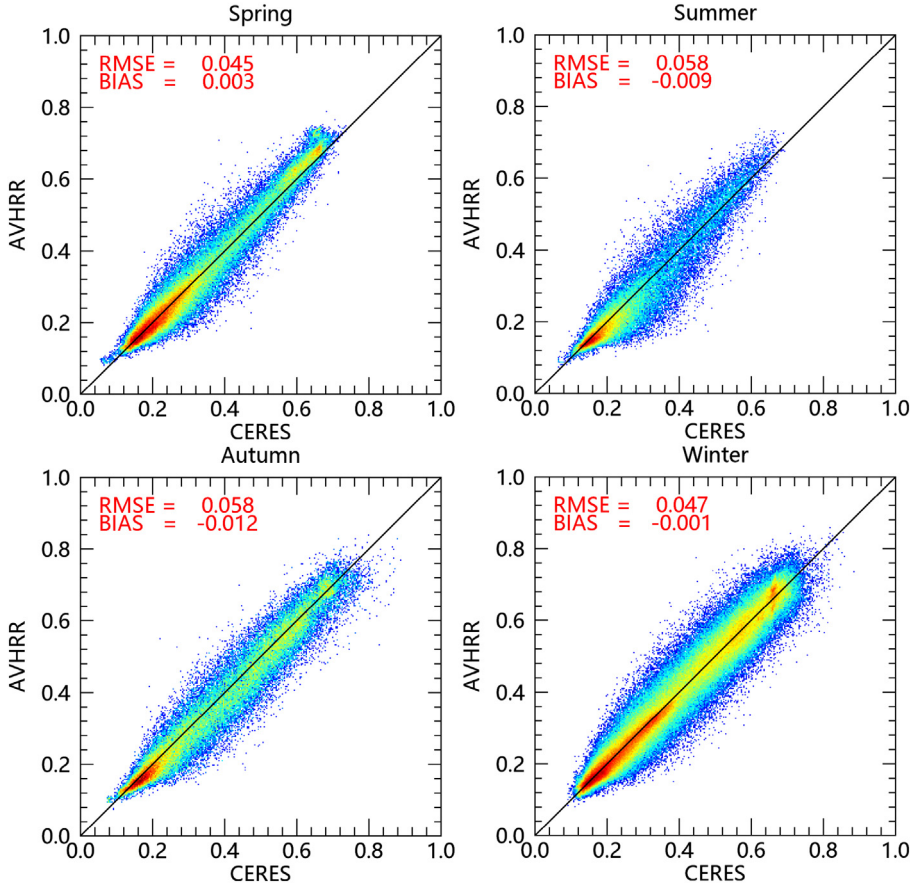

Fig. 6. Same with Fig. 5 but for spring, summer, autumn and winter in all sky conditions.

distributions among them. Clear-sky models produced smaller RMSE values comparing with the others, only around 0.010 at small SZA (< 70°), followed by snow-cover models, generating a RMSE of around 0.020. The cloudy-sky models showed poorer fitting result in terms of RMSE but most of the values ranged from 0.015 to 0.035.

4.1.2. Usability of conversion ratios for daily/monthly mean TOA albedo

Compared to the instantaneous TOA albedo, daily/monthly mean values are of greater value to long-term climatic studies. Conversion ratios were built as described in Sections 3.2 and 3.3 to correct the diurnal variations for the daily mean TOA albedo and thereby monthly mean TOA albedo.

Given specific atmospheric conditions, the diurnal curve of TOA albedo is a function of the solar zenith angle (Rutan et al., 2014; Wang et al., 2005) while the changes in atmospheric conditions within a single day is another factor that controls the diurnal variations. Based on the 3-hourly diurnal cycles, the climatology conversion ratio and real-time conversion ratio both take into account the changes of atmospheric conditions and the solar zenith angle while the real-time conversion ratio is expected to provide more accurate diurnal variations due to its dependence on real-time observations. However, as the real-time conversion ratio was only available after 2000, for the long-term data generation, the climatology conversion ratio was then applied. In order to investigate the usability of the climatology conversion ratio, we calculated the daily/monthly mean TOA albedo based on both of the two ratios. The results from real-time conversion ratio were taken as the references and the differences of the two retrievals were then calculated as the uncertainties brought by the climatology conversion ratio (Fig. 3).

For the daily mean TOA albedo (Fig. 3a), the largest differences are seen in the tropics (from −20° to 10°) and the eastern United States. Note that changes in cloud cover constitute the dominant variations in the atmosphere, and the convective cloud cover over land may change rapidly in the tropical and coastal regions. Compared with the real-time conversion ratio, the climatology ratio may not be able to capture some real-time changes, which did not occur periodically and could not be predicted based on the historical diurnal cycles. However, on the monthly scale, much smaller differences were found between the results derived from these two ratios (Fig. 3b). The largest difference was < 0.05 around the equatorial region. For monthly products, the diurnal variations among different days compensated for each other and were dominated by the relatively stable periodic changes from year to year. As such, the effects of differences between the two ratios were not as significant as they were on the daily scale.

To obtain a comprehensive estimation for the effects of the two ratios in producing monthly TOA albedo, the differences by the two ratios for all the twelve months in 2008 were calculated (Fig. 4). In general, the differences between the results based on the two ratios followed a Gaussian distribution and showed no systematic bias. Most of the differences (97.6%) were within 0.02, 86% of them were below 0.01 and all of the differences were below 0.05.

In a short summary, on the daily scale the climatology conversion ratio may fail to capture the actual diurnal variations at tropical and coastal regions but work well at other regions. However, on a monthly scale the periodic variations dominate and the climatology conversion ratios could be used for global TOA albedo estimation with uncertainties < 0.05. In this study, we focus on the monthly mean TOA albedo in the long-term record.

4.2. Validation

Two datasets were used in the validation part: CERES and CM SAF.

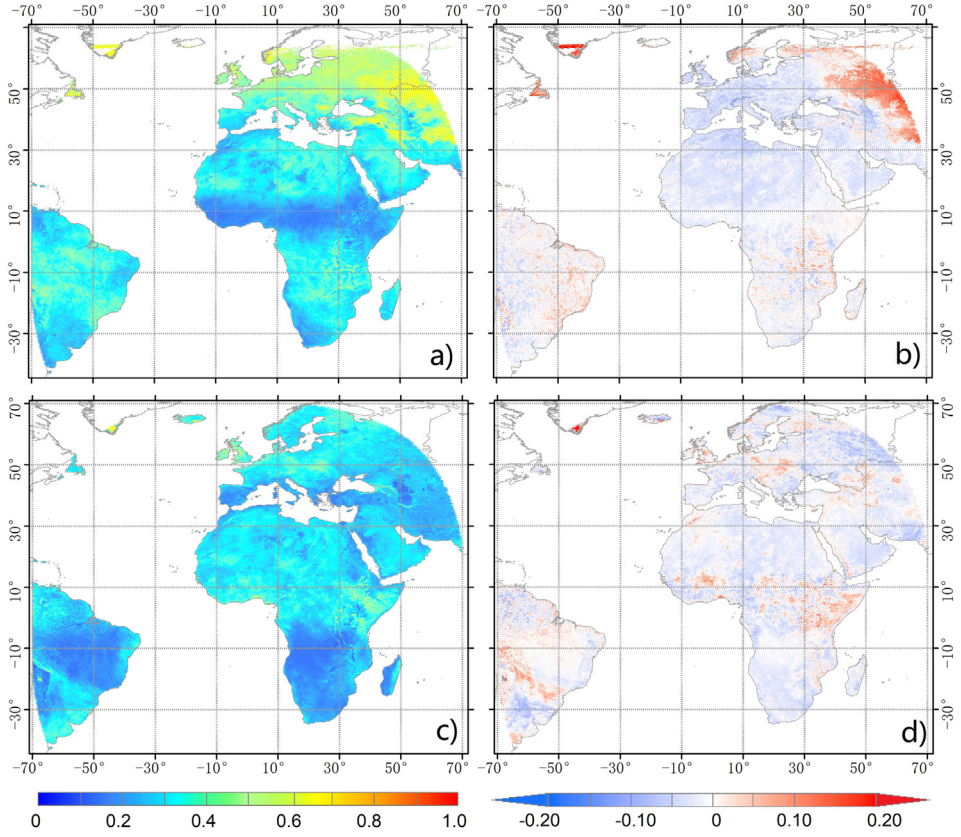

Fig. 7. Monthly mean TOA albedo in January 2008 for a) TAL-AVHRR b) differences between TAL-AVHRR and CM SAF and in July 2008 for c) TAL-AVHRR and d) differences between TAL-AVHRR and CM SAF.

The CERES product has been recognized as the most reliable TOA broadband flux dataset and therefore it was employed as the main reference for validation. CM SAF has the same spatial resolution (0.05°) as our product and, thus, is taken as the additional source at higher resolution for further validation. CERES provided both instantaneous product CERES SSF (Level-2 product at 20 km × 20 km) and daily/monthly mean product CERES SYN (Level-3 product at 1° × 1°). We first compare the instantaneous TAL-AVHRR with CERES SSF and then validate the monthly mean dataset by both CERES SYN and CM SAF.

4.2.1. Instantaneous TOA albedo

To investigate the overall performance of the instantaneous values, twelve-day TOA albedos in 2008 (one day for each month) were calculated. The 0.05° AVHRR pixels were first aggregated within a 20 km × 20 km CERES footprint and then the coincident and co-angled data pairs were selected for the comparison. Validations for all the selected data pairs are shown in Fig. 5a. Generally, TAL-AVHRR showed good consistency with CERES, with an overall RMSE of 0.047 and bias of −0.001 under all-sky conditions. To evaluate the accuracy of cloudy-sky model, clear-sky model and snow-cover model separately, we further divided our data pairs into different conditions. Note that the uncertainties of our final results may come from both the model itself and the accuracy of the ancillary input data, namely, cloud mask and snow mask. In this part, we intended to investigate the effectiveness of the model itself. Thus, it was essential to minimize the uncertainties brought about by the incorrect inputs. We took the clear/cloudy samples with consistent CERES and AVHRR cloud flag as pixels with high-confidence inputs and only these pixels were employed in our validation. The overall validation results for cloudy-sky and clear-sky conditions were illustrated in Fig. 5b and Fig. 5c. Obviously, the clear-sky model performed better than the cloudy-sky model in terms of RMSE (Fig. 5b,c). The cloudy-sky conditions exhibited small underestimation especially at low values. In contrast, the clear-sky conditions showed a slight overestimation at high end values. To investigate the possible reason, we further separated them to three main land cover types, including vegetation, desert and snow (Fig. 5d,e,f). Similar to the principle of cloudy/clear sample identification, the most reliable data source MODIS land cover, MODIS real-time snow cover and AVHRR real-time snow cover were collected to distinguish different land cover types. It is noted that the results for the vegetation and desert regions agreed quite well with CERES, with RMSE < 0.016. The results for snow region yielded a larger RMSE at 0.035 (6.7%, mean value = 0.526) and showed a slight positive bias at 0.019. However, the snow-cover TOA albedo were still controversial and previous studies had reported that CERES data may underestimate the snow and ice cover by 5% (Hudson et al., 2010; Hudson et al., 2010). Thus, our overestimation comparing with CERES may suggest a more reasonable retrieval over snow region. Overall, the validation showed that our models for instantaneous TOA albedo are robust for clear sky (snow-free), cloudy sky and snow cover regions.

The models for the instantaneous TOA albedo have been proven to be successful. However, the errors from the input ancillary data may also bring uncertainties to the final results. We have shown the overall accuracy for all the instantaneous data pairs in Fig. 5a. Here, four seasons representing different atmospheric conditions were validated separately in Fig. 6 (spring stands for March–April-May, summer for June–July-August, autumn for September–October-November and winter for December–January–February). Among the four seasons, better performance was found in spring and winter, with RMSE at 0.045 and 0.047, respectively. Underestimation occurred in summer (bias = −0.009) and autumn (bias = −0.012) and the low-end values mainly contributed to this underestimation. The underestimation of the cloudy-sky model (Fig. 5b) and the uncertainties from the input data may both contribute to this bias. Further analysis would be discussed in

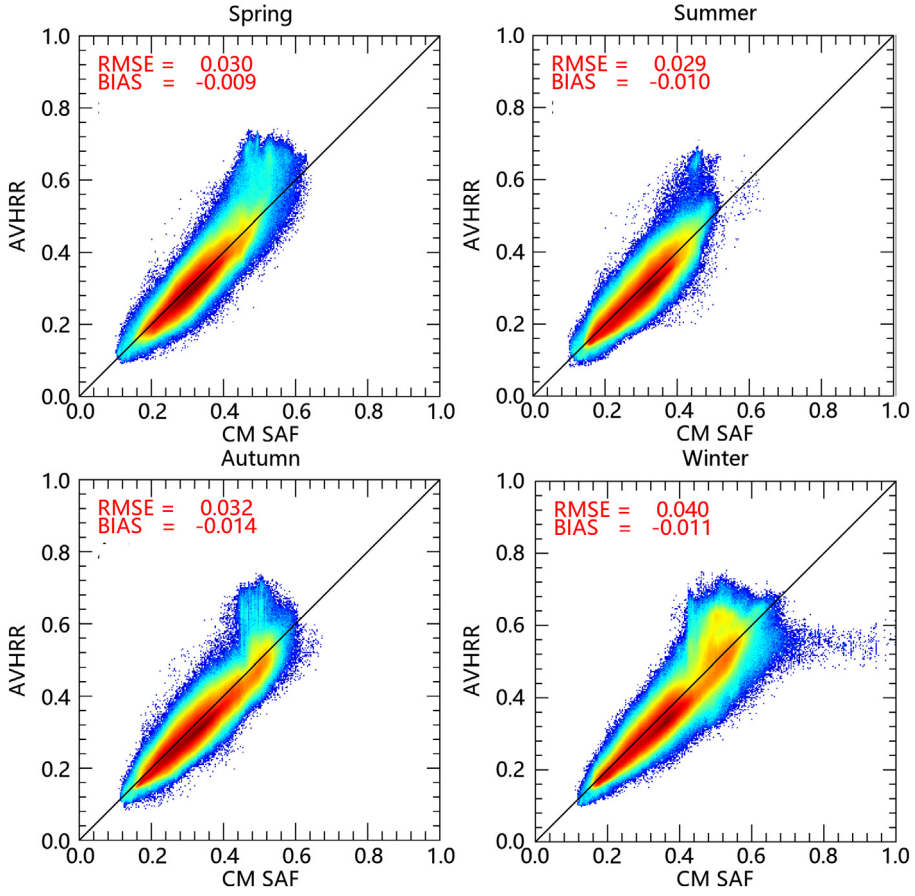

Fig. 8. Monthly mean TAL-AVHRR comparison with CM SAF at 0.05° × 0.05°in 2008 for spring, summer, autumn and winter.

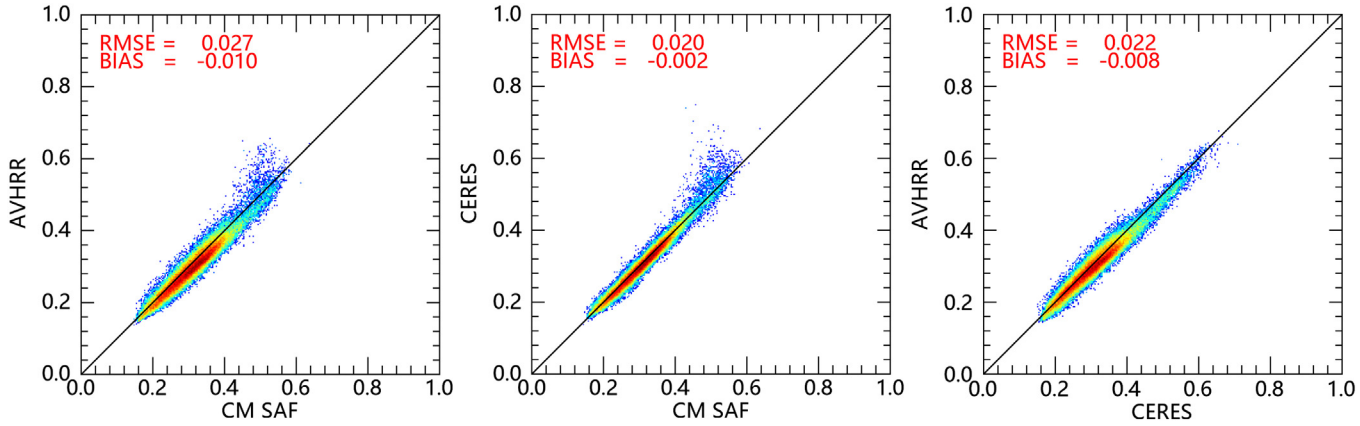

Fig. 9. Cross comparison among TAL-AVHRR, CM SAF and CERES at 1° × 1° for monthly mean TOA albedo in twelve months of 2008.

Section 5.

4.2.2. Monthly mean TOA albedo

Two datasets were chosen to validate the monthly mean TOA albedo: (1) CM SAF radiation dataset providing the same spatial resolution as TAL-AVHRR at 0.05° but only at limited spatial coverage. (2) CERES SYN L3 data with global coverage but at coarse resolution of 1°.

TAL-AVHRR agreed well with CM SAF with differences < 0.05 except some high latitude regions (Fig. 7). Among the four seasons, spring demonstrated the best performance with a RMSE = 0.030 and bias = −0.009, while all the other seasons also had an overall RMSE lower than 0.040 (Fig. 8). The overestimation found at the high-end values for winter seasons (Fig. 8) was corresponding to the high latitude region (latitude > 30°) in Fig. 7.

An inter-comparison among the three datasets were also conducted to further investigate the results (Fig. 9). CM SAF and TAL-AVHRR were both aggregated to the CERES 1° × 1° grid before the comparison. The coarse resolution results between CM SAF and TAL-AVHRR had better agreements comparing with the results at 0.05° due to the uncertainties mitigation and compensation at larger grids. All the three datasets matched each other quite well, with RMSE ranging from 0.020 to 0.027 and absolute bias ranging from 0.002 to 0.010. It is noted that at the high-end values TAL-AVHRR and CERES had better agreement with each other and both of them overestimated comparing with CM SAF.

The evaluation by CM SAF was only limited to 70°N–70°S, 70°W–70°E. To perform a comprehensive validation, our results were

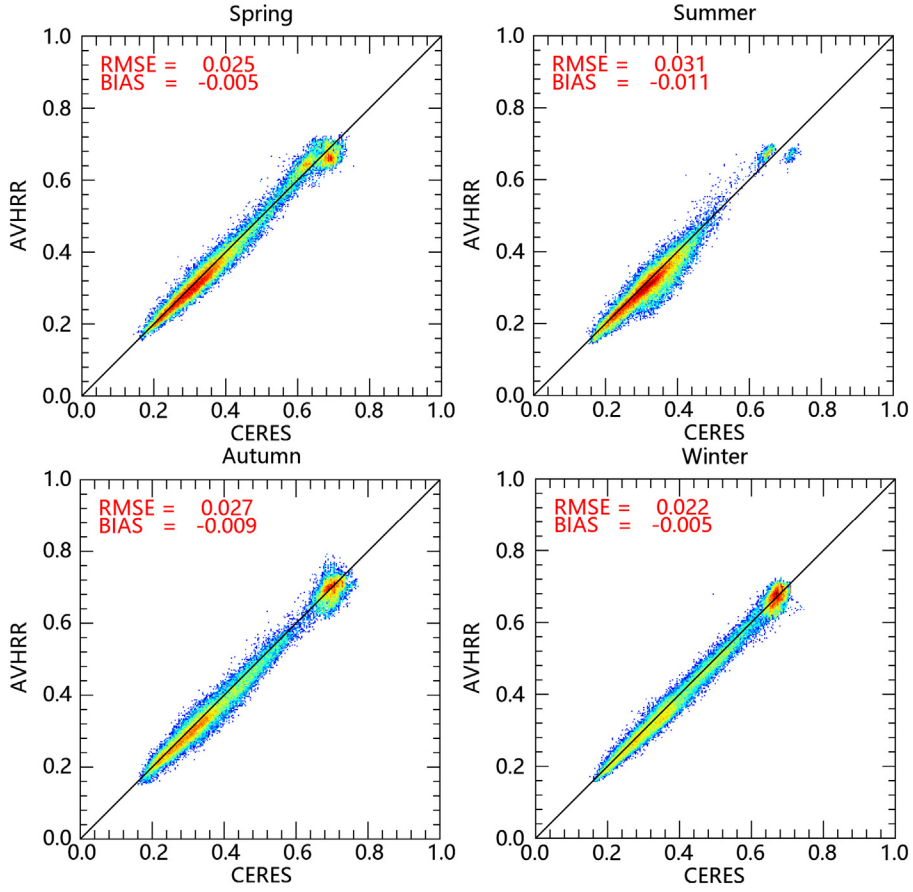

Fig. 10. Monthly mean TAL-AVHRR comparison with CERES at 1° × 1° in 2008 for spring, summer, autumn and winter.

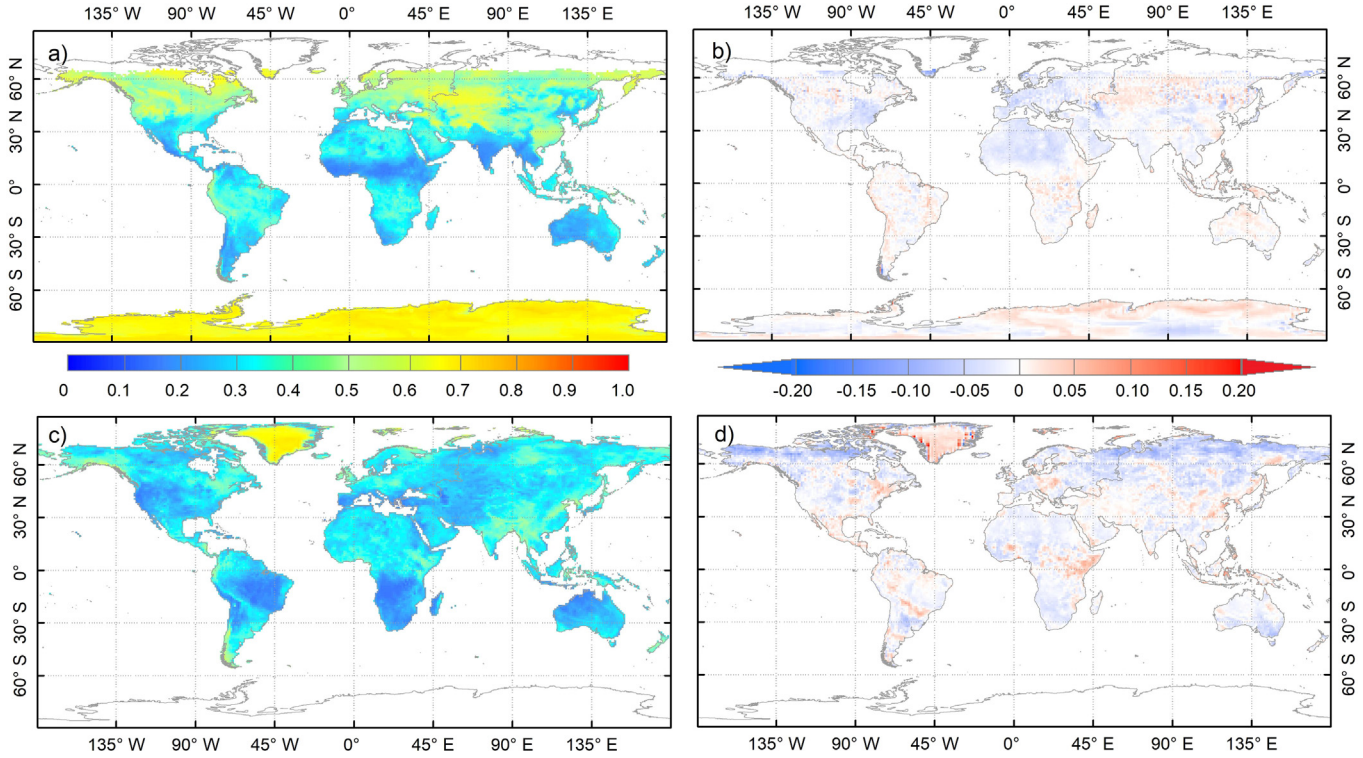

Fig. 11. Monthly mean TOA albedo in January 2008 for a) TAL-AVHRR b) differences between TAL-AVHRR and CERES and in July 2008 for c) TAL-AVHRR and d) differences between TAL-AVHRR and CERES.

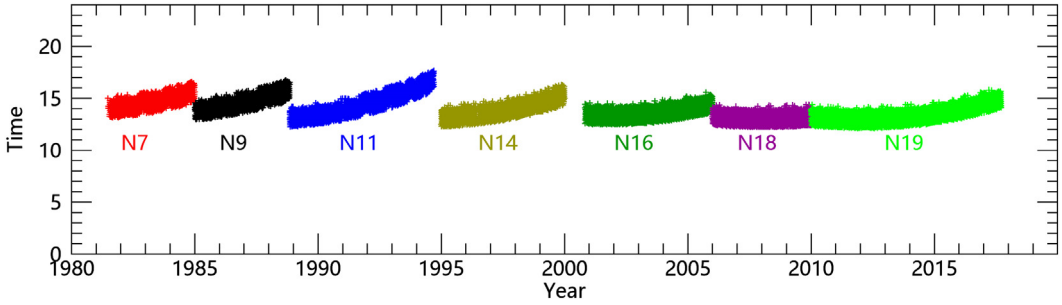

Fig. 12. Local time of the AVHRR measurements in use for the location 28.9 N, 23.8E in Libyan. The near terminator observations were removed and the measurements from the following satellite were used.

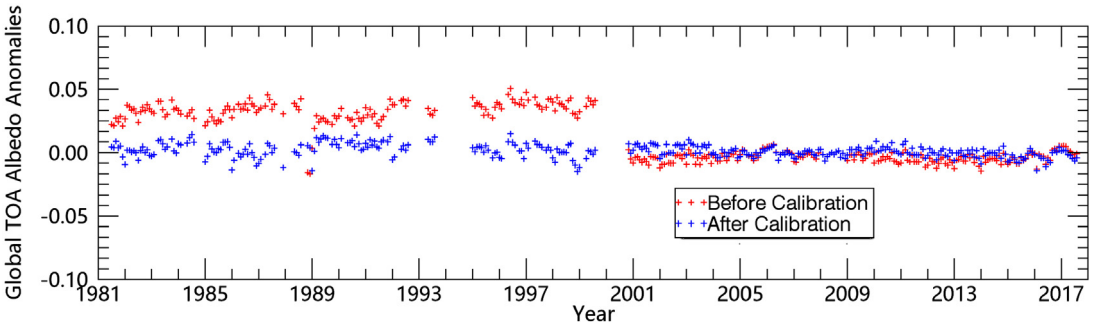

Fig. 13. Global deseasonalized monthly mean albedo anomalies before and after pseudo-invariant calibration. The months with spatial coverage < 90% were removed.

also compared with CERES SYN for 12 months in 2008, globally. The two datasets showed good agreement with each other (Fig. 10), with RMSE ranging from 0.22 to 0.31 at different seasons. Summer and autumn illustrated a relatively larger negative bias than spring and winter, which was also found in the instantaneous results (Fig. 6). Fig. 11 displayed the global TOA albedo maps for January and July of 2008. Overall, the two datasets matched well with each other in both January and July. However, consistent with the statistics in Fig. 10, January (winter time) showed better agreement than July (summer time). The main discrepancies in July occurred at the high latitude region, where the TAL-AVHRR displayed lower values than CERES and accounted for the overall underestimation.

4.3. Long-term TOA albedo from 1981 to 2017

The long-term TOA albedo is very important to climatic or ecological studies; the proposed algorithms were applied to AVHRR data to produce such a long-term TOA albedo record from 1981 to 2017. However, systematic inconsistencies were found between different satellite platforms due to changes of sensor design and sensor degradation, and this inconsistency was pronounced especially before and after 2000 when AVHRR-2 was transferred to AVHRR-3 (Latifovic et al., 2012; Molling et al., 2010; Tian et al., 2015). Thus, we employed an effective method, pseudo-invariant calibration sites (PICS) approach, to correct the inter-annual calibration inconsistency across AVHRR sensors (Bhatt et al., 2016; Heidinger et al., 2010). The assumption of this method is that some natural ground targets, such as desert and permanent snow/ice surface, kept stable and therefore could be used as the references for calibration. Based on the evaluation of previous studies (Bhatt et al., 2016; Uprety and Cao, 2011), six most suitable sites, including four desert sites (Libya-1, Libya-4, Arabia-1, Niger-1) and two polar icecap sites (Dome-C, Greenland), were selected for the calibration.

The calibration was based on the monthly mean TOA albedo, which had corrected the BRDF effect and the diurnal variations. At the first step, a 9 × 9 window (0.45° × 0.45°) was used for all the six sites. For each site, to mitigate the noise, the median values were selected from the clear-sky pixels in the 9 × 9 window for each month from 1981 to 2017. Among the good calibration years after 2000, the AVHRR onboard NOAA-18 were the most stable satellite and the year 2008 had the smallest variations of the observation time (Fig. 12). Therefore, we took the values from 2008 as the reference for the calibration by month. In the following step, a set of coefficients was developed for each year, by regressing the TOA albedo of the corresponding year at the invariant sites to the reference values calculated in the second step. Finally, the coefficients were applied to each satellite to generate the daily and monthly mean long-term data record.

The long-term datasets were more consistent after the calibration (Fig. 13). The improvements were significant especially at mitigating the large discrepancy of the years before 2000 and after 2000 caused by the changes of the sensor design. Slight adjustments were also found for NOAA-16 and NOAA-19 era at 2000–2005 and 2010–2016 respectively, which eliminated the calibration differences of different satellites. Note that the months in the late 1984, 1993–1994 and 2000 had some data gaps due to the unavailability of source data.

Based on the calibrated long-term data record, regional mean TOA albedo anomalies were calculated from 1981 to 2017 (Fig. 14), and the data were also compared with CERES for the overlap period from 2000 to 2017. The absolute differences between AVHRR and CERES were calculated for different latitude zones. The region covering 30° to 60° showed the smallest relative RMSE at 1.9%, followed by the region from −60° to −30° and the one from 0° to 30° with relative RMSEs of 2.7% and 3.2%, respectively. The area covering −30° to 0° displayed a poorer accuracy than other latitude zones, but still at 4.5%, corresponding to the value at 0.012. Even though the tropical region displayed some overestimations comparing with CERES, the deseasonalized albedo anomalies, which were indicators of climate change, agreed closely with CERES for different latitude regions. This suggested that the underestimation or overestimation in our dataset were seasonally or regionally dependent and could be removed after the deseasonalizing process. Some short periods at the satellite terminating stage, such as 2015–2017 for −30° to 0°, 1998–1999 for 0°-30°,

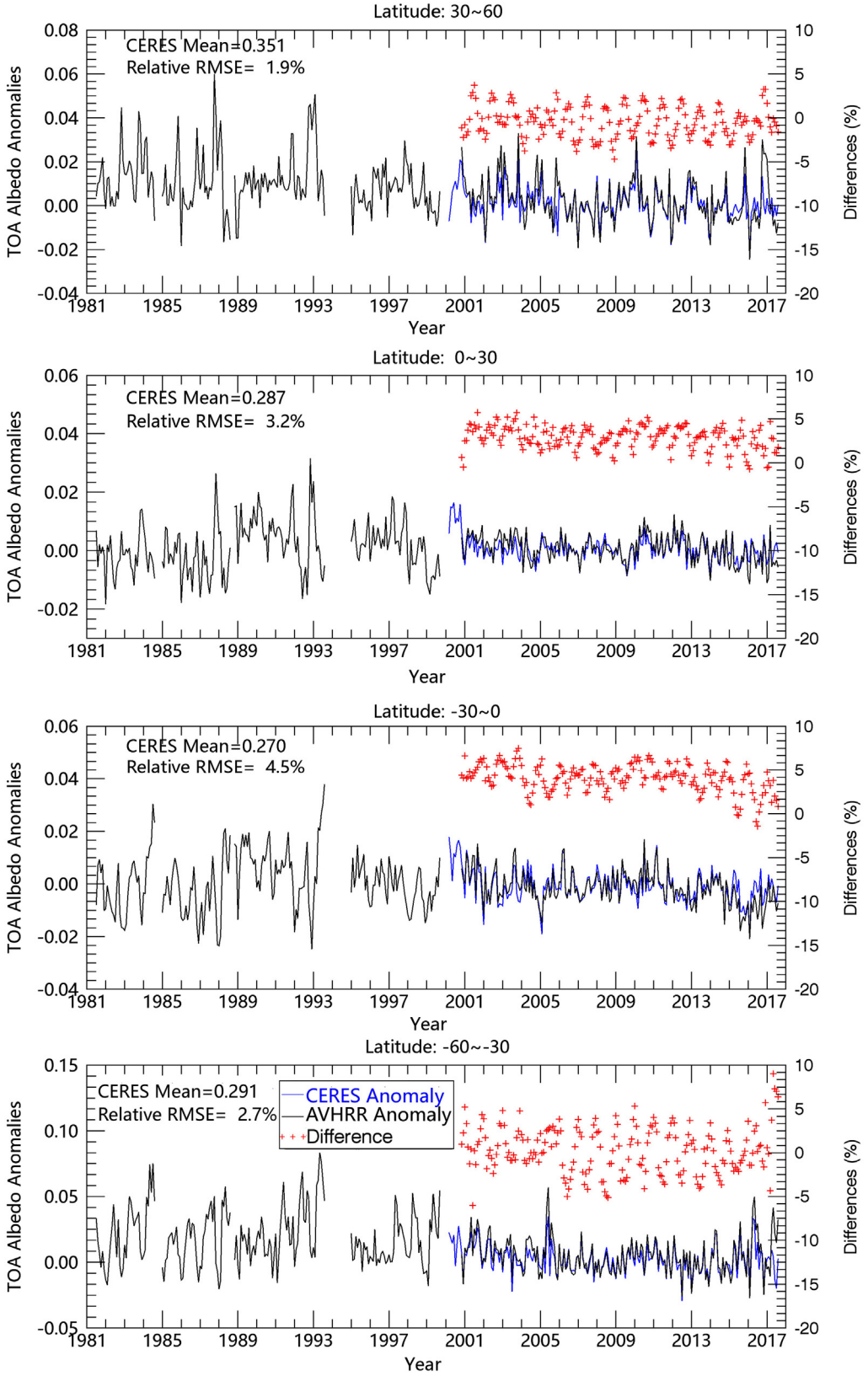

Fig. 14. AVHRR and CERES monthly mean TOA albedo anomalies with a common base period 2006–2009 (black and blue solid line, respectively). The absolute differences were calculated between the AVHRR and CERES monthly mean TOA albedo (red dot) in the overlap period from 2000 to 2017. The months with spatial coverage < 90% were removed. (For interpretation of the references to colour in this figure legend, the reader is referred to the web version of this article.)

1991–1993 for −60° to −30°, still showed some small spurious trends, which may be related to the residual orbit shift issues of NOAA-19, NOAA-14 and NOAA-11, caused by the poor data quality, the insufficient diurnal samples and diurnal correction methods. However, both the absolute biases and short period spurious trends had little impact on the trends detection and our dataset showed stability in

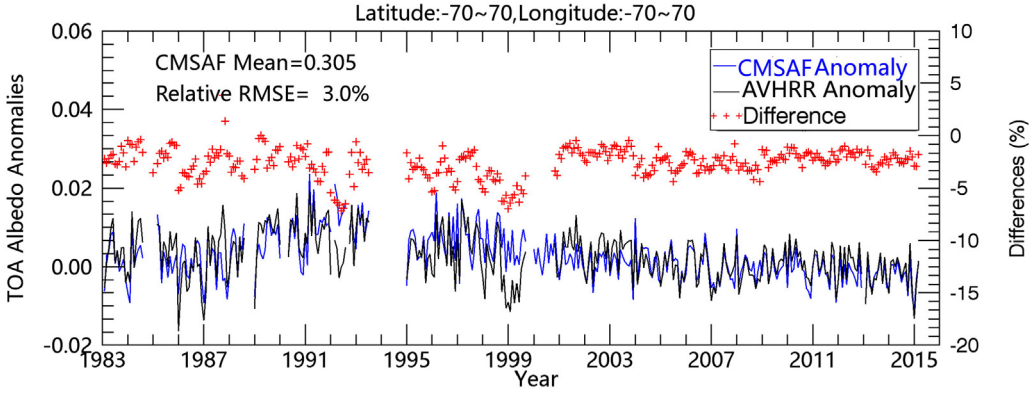

Fig. 15. AVHRR and CM SAF monthly mean TOA albedo anomalies from 1983 to 2015 with a common base period 2006–2009 (black and blue solid line, respectively). The absolute differences were calculated between the AVHRR and CM SAF monthly mean TOA albedo (red dot). The months with spatial coverage < 90% were removed. (For interpretation of the references to colour in this figure legend, the reader is referred to the web version of this article.)

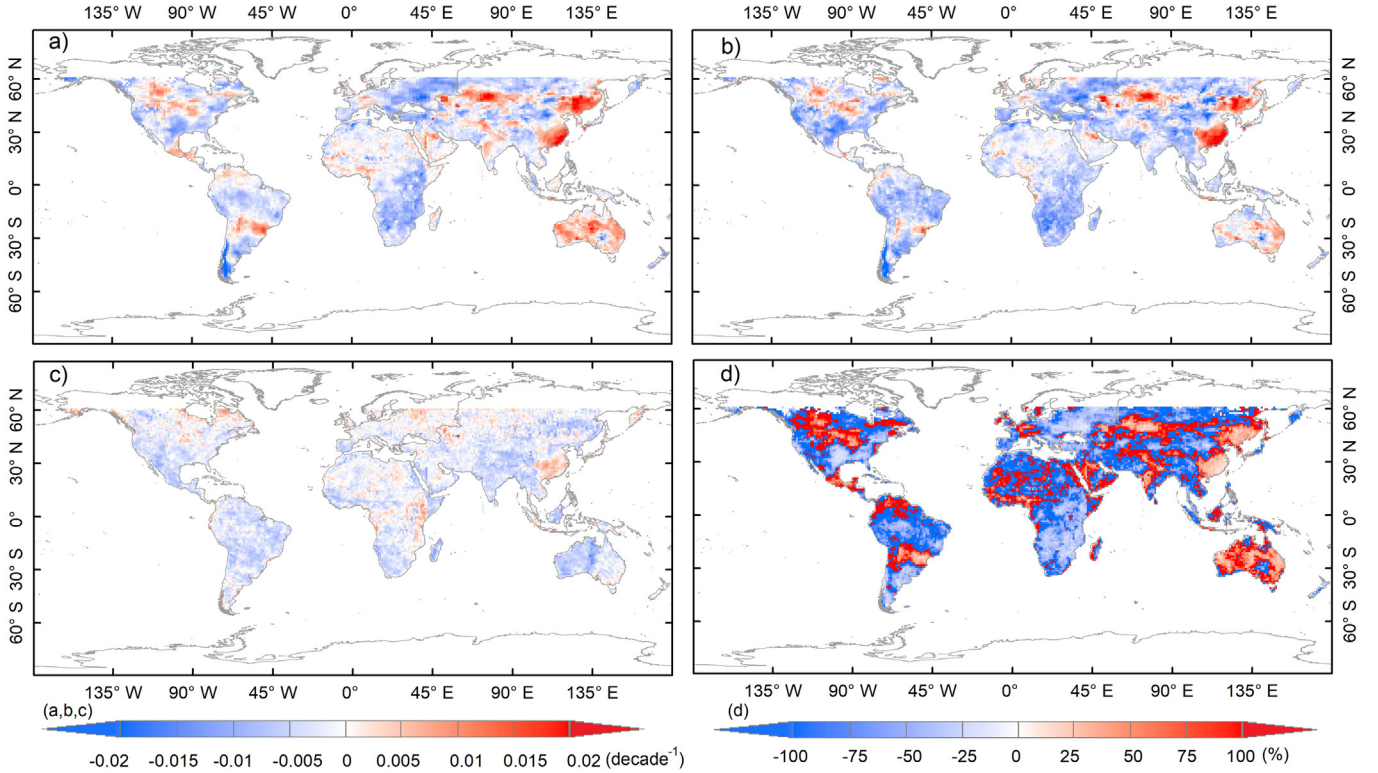

Fig. 16. Trend of deseasonalized monthly mean TOA albedo anomalies from 2001 to 2016 based on a) CERES EBAF and b) TAL-AVHRR; c) anomaly differences between TAL-AVHRR and CERES EBAF; d) ratio of the standard deviation of 0.05° × 0.05° TAL-AVHRR trend within 1° × 1° grid and the co-located CERES EBAF trend.

revealing the climate anomalies after 2000 comparing with CERES data.

To validate the results before 2000, CM SAF TOA shortwave flux data from Feb.1983 to Mar.2015 were employed for further evaluation (Fig. 15). A relative RMSE of 3.0% was found and the long-term differences between our product and CM SAF in the last several decades were stable except the drops during 1992 and 1999. The drops in 1999 may be a result of residual bias caused by the imperfect diurnal correction of AVHRR in the terminating era of NOAA-14 while the disagreement in 1992 was possibly related with the bias in CM SAF due to the discontinuity of CM SAF data around 1992. However, the albedo anomalies from the two datasets matched very well with each other overall and both showed increase trend till 1996 and decrease trend afterwards.

Moreover, to have a full understanding of our dataset in quantifying the climatic variations in global scale, the trends of deseasonalized albedo anomalies from 2001 to 2016 were calculated in 1° × 1° grid based on both TAL-AVHRR and CERES Energy Balanced and Filled (EBAF) product. The results from these two datasets showed very similar spatial pattern (Fig. 16.a, b), with significant increase in the north and southeast of China and Kazakhstan. AVHRR generally demonstrated slightly larger trend magnitude than CERES, specifically, overestimated the positive trends and underestimated the negative trends, but within 0.005/decade (Fig. 16.c). In order to investigate the ability of TAL-AVHRR at detecting the spatial details, we calculated the standard deviation of 0.05° × 0.05° TAL-AVHRR trend within each 1° × 1° grid and compared them with the co-located CERES trend. The spatial variability of the AVHRR trend was even greater than the 1° × 1° CERES trend (ratio > 100% or ratio < −100% in Fig. 16.d) and demonstrated more details in the regions with small trend values or dramatic trend variations. Comparing with 1° × 1° CERES data, the 0.05° × 0.05° TAL-AVHRR provided more details in terms of the trend variability.

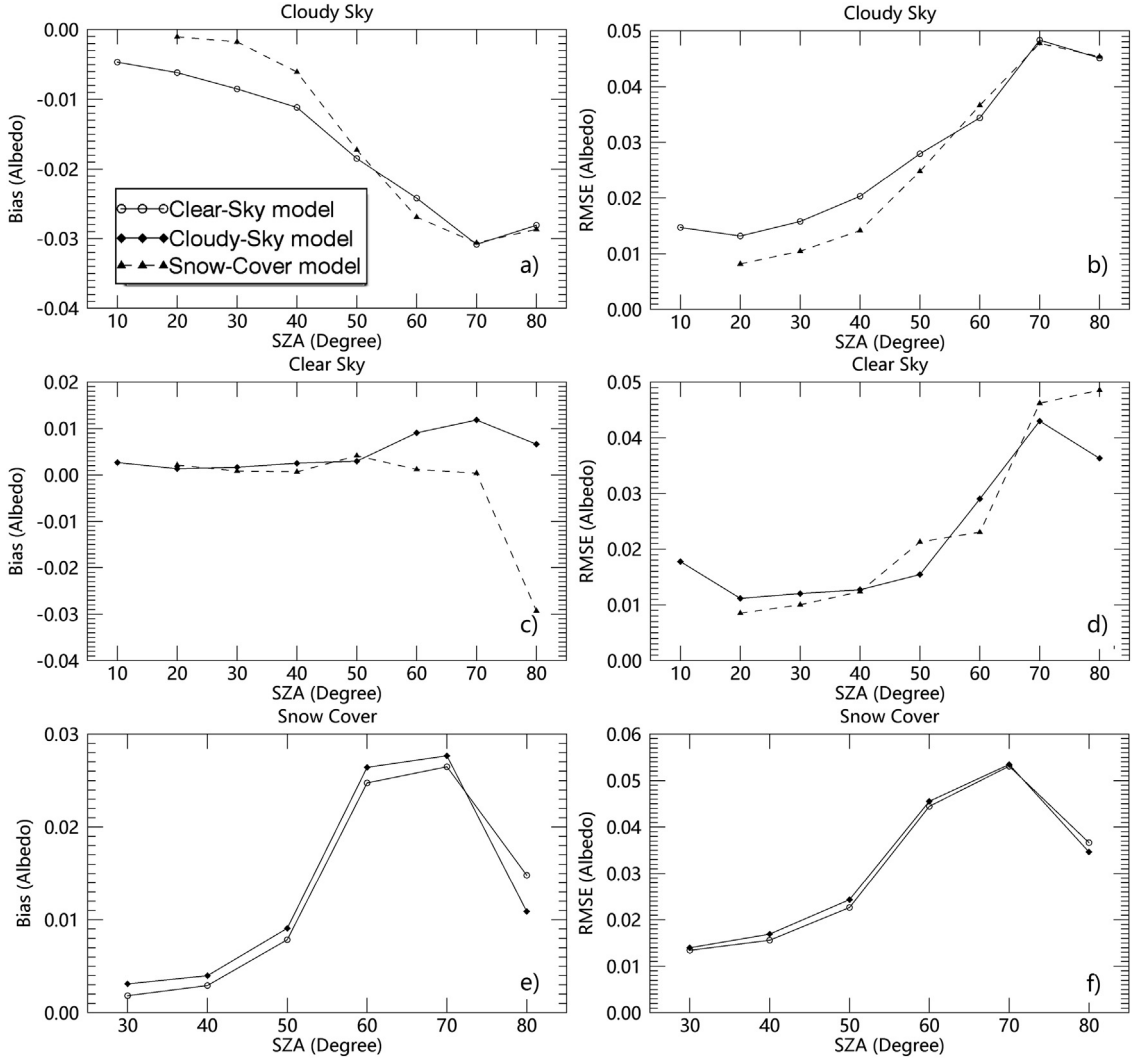

Fig. 17. The bias and RMSE for the incorrect models applying under (a) (b)cloudy sky (c) (d) clear sky and (e) (f)snow cover.

5. Uncertainties and limitations

5.1. Uncertainty analysis for the instantaneous TOA albedo

It is desirable to build a direct relationship between AVHRR observations and high-resolution TAL-MODIS and we have obtained high accuracy instantaneous products based on the framework. Even though this method may have limitations at tracing back the mixed uncertainties from different sources, including the TAL-MODIS, the training method and the input data, the uncertainties from different sources could be quantified. The accuracy of the TAL-MODIS and the fitting accuracy of the training method were both transferred to the performance of our models, which had been identified in Section 4.1. Here, we mainly focus on analyzing the uncertainties from the input data, specifically, the AVHRR cloud mask and snow mask.

To trace the uncertainties from the input data, MODIS cloud and snow masks, which were reported to have high accuracy, were employed to produce a reference dataset. Specifically, MODIS near-coincident (< 5-minute interval with AVHRR) cloud and snow masks were taken as inputs instead of the AVHRR masks, thereby, producing a control dataset (hereafter AVHRR reference). The differences between the AVHRR TOA albedo and AVHRR reference were regarded as the uncertainties brought by the input data. Except for those consistent inputs, which AVHRR and MODIS both flag as clear-sky, cloudy-sky or snow cover, we separated the inconsistent cases into different groups. Under a cloudy sky (which is classified as cloud by MODIS mask but regarded as clear or snow by AVHRR mask), the incorrect inputs may lead to the use of the clear-sky model or snow-cover model (Fig. 17a,b). Similarly, we had incorrect cases for clear-sky (Fig. 17c,d) and snow-cover cases (Fig. 17e,f).

Generally, the biases caused by the incorrect input increased with SZA (except for SZA > 70°), but they were all < 0.03 and the RMSE were lower than 0.06. Among the three conditions, clear-sky (snow-free) showed the smallest RMSE and bias (Fig. 17c,d). In other words, an incorrect clear-sky classification resulted in a smaller bias than other incorrect cases. And if the clear sky was misclassified as cloudy sky, the bias would be positive while if the clear sky was recognized incorrectly as snow cover, the bias was close to 0 and negligible (except for SZA > 70°). For cloudy sky, applying an unmatched clear-sky model or snow-cover model would lead to a negative bias (Fig. 17.a) and for snow cover, an incorrect cloudy-sky and clear-sky model would produce a positive bias. That is to say, less (more) cloud recognition (cloudy sky recognized as clear sky or snow cover) tend to underestimate (overestimate) the results (Fig. 17.b) and less (more) snow cover (snow cover recognized as clear/cloudy) led to the overestimation (underestimate) of the retrieval (Fig. 17.f).

To identify the possible biases caused by the input data, the fractions for cloudy-sky, clear-sky and snow-cover were calculated from MODIS and AVHRR inputs separately (Table 3). It was noted that the most significant discrepancy occurred in the cloud misclassification.

Table 3
Cloudy-sky, snow-cover and clear-sky (snow-free) fractions based on coincident MODIS and AVHRR cloud and snow masks in 2008.

	Spring	MODIS (%)				Summer	MODIS (%)			
		Cloud	Snow	Clear	Total		Cloud	Snow	Clear	Total
AVHRR (%)	Cloud	59.07	*1.18*	*6.74*	66.99	Cloud	56.30	*0.29*	*6.14*	62.73
	Snow	**3.16**	9.93	0.12	13.20	Snow	**0.88**	0.34	0.05	1.27
	Clear	**8.53**	0.10	11.18	19.80	Clear	**16.32**	0.10	19.58	36.00
	Total	70.76	11.20	18.03	–	Total	73.50	0.73	25.77	–
	Autumn	MODIS (%)				Winter	MODIS (%)			
		Cloud	Snow	Clear	Total		Cloud	Snow	Clear	Total
AVHRR (%)	Cloud	65.52	*0.79*	*6.34*	72.65	Cloud	47.97	*1.73*	*3.83*	53.53
	Snow	**5.20**	1.55	0.10	6.85	Snow	**11.45**	8.80	0.15	20.41
	Clear	**8.78**	0.09	11.63	20.50	Clear	**12.47**	0.09	13.50	26.06
	Total	79.50	2.43	18.07	–	Total	71.89	10.62	17.48	–

*The numbers with bold type represent the underestimation cases of AVHRR cloud fraction and the numbers with italic type represent the overestimation cases of AVHRR cloud fraction.

Specifically, AVHRR underestimated the cloud fraction for all the seasons and applying the clear-sky or snow-cover model incorrectly under cloudy-sky condition would both lead to underestimation (Fig. 17a). Thus, the underestimation of cloud fraction may be one of the reasons for the overall slight underestimation in our products. Moreover, applying the clear-sky model would result in an even larger bias than using the snow-cover model under cloudy sky. Among the four seasons, summer had the largest error proportion (16.32%) in misclassifying the cloudy-sky to clear-sky, which may suggest the reason of the largest negative bias in summer time (Fig. 10).

5.2. Uncertainty for the daily/monthly mean TOA albedo

The instantaneous TOA albedo were converted to daily mean values and then integrated to the monthly mean values. The uncertainties of daily/monthly mean TOA albedo comes from both the instantaneous retrievals and the instantaneous-to-daily correction process. Building conversion ratio was the key for the diurnal variation correction. To produce a long-term data record, climatology conversion ratio was developed for the entire time series. As we have discussed in 4.1.2, based on the climatology ratio, large uncertainties (~0.2) may occur in the retrieval of daily mean TOA albedo while the uncertainties of monthly mean values were basically within 0.02 at pixel level. The instantaneous TOA albedo uncertainties were at the level of ~0.01. Mixing the biases from both the instantaneous retrievals and the diurnal correction process, the monthly mean TOA albedo were found a bias at ~0.01 level for different seasons. To further mitigate the calibration inconsistency between different sensors, PICS approaches were used to generate the long term series dataset. The calibrated long-term TAL-AVHRR showed < 5% relative RMSE comparing with the other two TOA albedo datasets.

It is a challenge to produce a long-term dataset which is useful at revealing the trends of climate change in regional and global scale. Our monthly mean TAL-AVHRR were validated to have comparable capacity with CERES and CM SAF at detecting the anomaly variations for different latitude zones. At 1° × 1° grid level, the trend spatial pattern based on TAL-AVHRR and CERES agreed very well with each other and the trend differences were within 0.005/decade.

We are collecting recently published CERES hourly flux data. In the next step, more advanced diurnal models, such as the sinusoidal harmonic functions (Foster and Heidinger, 2013; Lee et al., 2007), will be employed to improve the accuracy of the daily and monthly mean product. On the other hand, multiple observations in a single day would also help to capture the diurnal dynamics, thus, including other AVHRR fundamental data records PATMOS-x (Heidinger et al., 2014) will further improve the results.

6. Summary

TOA albedo is a critical parameter for both climate models and climate change studies. AVHRR provides a unique global data source for long-term TOA albedo generation since 1981. In this study, based on multispectral AVHRR data, we proposed a robust method for estimating the instantaneous and daily/monthly mean TOA albedo. A direct estimation algorithm was built to derive instantaneous TOA albedo, which were subsequently converted to daily/monthly mean TOA albedo. The essence of the direct estimation is to rely on spectral information to correct the anisotropic effect for different scene types, mitigating the uncertainties brought by the scene type definition and ADM development. The method is suitable for global implementation, as only a cloud mask and a snow mask are needed as the ancillary data. The diurnal variations were corrected by diurnal curves based on multi-year CERES 3-hourly flux data and the calibration inconsistency between different sensors was further corrected by the invariant targets.

The widely-used CERES data and high spatial resolution CM SAF data were employed to evaluate our products. The instantaneous TAL-

AVHRR showed an overall RMSE of 0.047 and a bias of −0.001 comparing with CERES at ~20 km footprint. Monthly mean TAL-AVHRR matched well with the regional CM SAF dataset at 0.05° × 0.05° and CERES at 1° × 1° with global coverage, with RMSE ranging from 0.029 to 0.040 and from 0.022 to 0.031, respectively. For AVHRR-based long term dataset, one of the obstacles was the inconsistency caused by the satellite orbit drift and calibration differences across the satellites. Our diurnal correction method and invariant target calibration were useful at mitigating the inconsistency. Even though some overall underestimations were found comparing with other datasets and the orbit drift residuals remained at some short periods of the satellite terminating stages for N11, N14 and N19, our monthly mean dataset showed comparable capacity with both of the reference datasets at detecting the trends at regional and latitudinal zones. The monthly mean TAL-AVHRR were recommended to the users for climate studies due to its high accuracy and good internal consistency.

It is noted that our methods correlated the AVHRR radiance and the broadband albedo, therefore, the datasets had limitations at detecting the spectral variations in the broadband albedo which had little correlation with the AVHRR observed channels. Other limitations include the overall underestimation and residual orbit drift effects. Future work includes the updates of more accurate ancillary datasets, such as snow mask and cloud mask, which will benefit the instantaneous TOA albedo retrieval. Incorporating higher temporal diurnal datasets and building more accurate diurnal models will be useful for the diurnal variation corrections and further mitigate the orbit drift effects in TAL-AVHRR dataset.

Acknowledgements

This study was partially funded by The National Key Research and Development Program of China (NO.2016YFA0600101) and the Chinese Scholarship Council. We thank GLASS science team in Beijing Normal University for providing the MODIS TOA albedo product, NASA/GSFC for providing AVHRR data and (https://ltdr.nascom.nasa.gov/) CERES data (https://ceres.larc.nasa.gov), CM SAF for CM SAF flux data (http://www.cmsaf.eu/) and JASMES for AVHRR snow cover data (http://kuroshio.eorc.jaxa.jp/JASMES/index.html). The first version of TAL-AVHRR (TAL-AVHRR V1.0) has been produced and updated to Aug, 2017 and the data are published at http://www.geodata.cn/ and http://glcf.umd.edu/data. We are very grateful for all the anonymous reviewers for their valuable comments and suggestions.

References

Ackerman, S.A., Holz, R.E., Frey, R., Eloranta, E.W., Maddux, B.C., McGill, M., 2008. Cloud detection with MODIS. Part II: validation. J. Atmos. Ocean. Technol. 25, 1073–1086.

Barkstrom, B.R., 1984. The earth radiation budget experiment (Erbe). Bull. Am. Meteorol. Soc. 65, 1170–1185.

Bhatt, R., Doelling, D.R., Scarino, B.R., Gopalan, A., Haney, C.O., Minnis, P., Bedka, K.M., 2016. A consistent AVHRR visible calibration record based on multiple methods applicable for the NOAA degrading orbits. Part I: methodology. J. Atmos. Ocean. Technol. 33, 2499–2515.

Chen, D., Loboda, T.V., 2018. Surface forcing of non-stand-replacing fires in Siberian larch forests. Environ. Res. Lett (in press).

Dewitte, S., Clerbaux, N., 2017. Measurement of the earth radiation budget at the top of the atmosphere—a review. Remote Sens. 9, 1143.

Dewitte, S., Clerbaux, N., Ipe, A., Velazquez, A., Baudrez, E., Nevens, S., Decoster, I., 2013. Climate monitoring with earth radiation budget measurements. Radiation Processes in the Atmosphere and Ocean Irs2012 (1531), 612–615.

Diner, D.J., Davies, R., Várnai, T., Moroney, C., Borel, C., Gerstl, S.A.W., Nelson, D.L., 1999. Level 2 Top-of-Atmosphere Albedo Algorithm Theoretical Basis.

Doelling, D.R., Loeb, N.G., Keyes, D.F., Nordeen, M.L., Morstad, D., Nguyen, C., Wielicki, B.A., Young, D.F., Sun, M., 2013. Geostationary enhanced temporal interpolation for CERES flux products. J. Atmos. Ocean. Technol. 30, 1072–1090.

Duvel, J.P., Viollier, M., Raberanto, P., Kandel, R., Haeffelin, M., Pakhomov, L.A., Golovko, V.A., Mueller, J., Stuhlmann, R., Grp, I.S.S.W., 2001. The ScaRaB-resurs earth radiation budget dataset and first results. Bull. Am. Meteorol. Soc. 82, 1397–1408.

Evans, R.H., Casey, K.S., Cornillon, P.C., 2010. Transition of AVHRR SST Pathfinder to Version 6, Continued Evolution of a CDR. American Geophysical Union, Miami, FL, USA.

Foster, M.J., Heidinger, A., 2013. PATMOS-x: results from a diurnally corrected 30-yr satellite cloud climatology. J. Clim. 26, 414–425.

Franch, B., Vermote, E.F., Roger, J.C., Murphy, E., Becker-Reshef, I., Justice, C., Claverie, M., Nagol, J., Csiszar, I., Meyer, D., Baret, F., Masuoka, E., Wolfe, R., Devadiga, S., 2017. A 30 + year AVHRR land surface reflectance climate data record and its application to wheat yield monitoring. Remote Sens. 9, 296.

Hall, D.K., Riggs, G.A., 2007. Accuracy assessment of the MODIS snow products. Hydrol. Process. 21, 1534–1547.

Harries, J.E., Russell, J.E., Hanafin, J.A., Brindley, H., Futyan, J., Rufus, J., Kellock, S., Matthews, G., Wrigley, R., Last, A., Mueller, J., Mossavati, R., Ashmall, J., Sawyer, E., Parker, D., Caldwell, M., Allan, P.M., Smith, A., Bates, M.J., Coan, B., Stewart, B.C., Lepine, D.R., Cornwall, L.A., Corney, D.R., Ricketts, M.J., Drummond, D., Smart, D., Cutler, R., Dewitte, S., Clerbaux, N., Gonzalez, L., Ipe, A., Bertrand, C., Joukoff, A., Crommelynck, D., Nelms, N., Llewellyn-Jones, D.T., Butcher, G., Smith, G.L., Szewczyk, Z.P., Mlynczak, P.E., Slingo, A., Allan, R.P., Ringer, M.A., 2005. The geostationary earth radiation budget project. Bull. Am. Meteorol. Soc. 86, 945–960.

He, T., Liang, S., Wang, D., Chen, X., Song, D.-X., Jiang, B., 2015. Land surface albedo estimation from Chinese HJ satellite data based on the direct estimation approach. Remote Sens. 7, 5495–5510.

Heidinger, A.K., Foster, M.J., Walther, A., Zhao, X., 2014. The pathfinder atmospheres-extended Avhrr climate dataset. Bull. Am. Meteorol. Soc. 95, 909–922.

Heidinger, A.K., Straka, W.C., Molling, C.C., Sullivan, J.T., Wu, X., 2010. Deriving an inter-sensor consistent calibration for the AVHRR solar reflectance data record. Int. J. Remote Sens. 31, 6493–6517.

Hori, M., Sugiura, K., Kobayashi, K., Aoki, T., Tanikawa, T., Kuchiki, K., Niwano, M., Enomoto, H., 2017. A 38-year (1978–2015) northern hemisphere daily snow cover extent product derived using consistent objective criteria from satellite-borne optical sensors. Remote Sens. Environ. 191, 402–418.

House, F.B., Gruber, A., Hunt, G.E., Mecherikunnel, A.T., 1986. History of satellite missions and measurements of the earth radiation budget (1957–1984). Rev. Geophys. 24, 357–377.

Hucek, R., Jacobowitz, H., 1995. Impact of scene dependence on Avhrr albedo models. J. Atmos. Ocean. Technol. 12, 697–711.

Hudson, S.R., Kato, S., Warren, S.G., 2010. Evaluating CERES angular distribution models for snow using surface reflectance observations from the East Antarctic plateau. J. Geophys. Res.-Atmos. 115.

Hudson, S.R., Warren, S.G., Kato, S., 2010. A comparison of shortwave reflectance over the East Antarctic Plateau observed by CERES to that estimated from surface reflectance observations. J. Geophys. Res.-Atmos. 115.

Jacobowitz, H., Soule, H.V., Kyle, H.L., House, F.B., 1984. The earth radiation budget (Erb) experiment — an overview. J. Geophys. Res.-Atmos. 89, 5021–5038.

Kandel, R., Viollier, M., Raberanto, P., Duvel, J.P., Pakhomov, L.A., Golovko, V.A., Trishchenko, A.P., Mueller, J., Raschke, E., Stuhlmann, R., ISSWG, I.S.S.W.G., 1998. The ScaRaB earth radiation budget dataset. Bull. Am. Meteorol. Soc. 79, 765–783.

Key, J.R., Wang, X.J., Stoeve, J.C., Fowler, C., 2001. Estimating the cloudy-sky albedo of sea ice and snow from space. J. Geophys. Res.-Atmos. 106, 12489–12497.

Latifovic, R., Pouliot, D., Dillabaugh, C., 2012. Identification and correction of systematic error in NOAA AVHRR long-term satellite data record. Remote Sens. Environ. 127, 84–97.

Lee, H.T., Gruber, A., Ellingson, R.G., Laszlo, I., 2007. Development of the HIRS outgoing longwave radiation climate dataset. J. Atmos. Ocean. Technol. 24, 2029–2047.

Liang, S., 2017. Remote sensing of earth's energy budget: an overview of recent progress. In: Liang, S. (Ed.), Comprehensive Remote Sensing. vol. 5. Elsevier, Oxford, UK, pp. 1–31 Earth's Energy Budget.

Liang, S., Stroeve, J., Box, J.E., 2005. Mapping daily snow/ice shortwave broadband albedo from Moderate Resolution Imaging Spectroradiometer (MODIS): the improved direct retrieval algorithm and validation with Greenland in situ measurement. J. Geophys. Res.-Atmos. 110.

Liang, S., Wang, K., Zhang, X., Wild, M., 2010. Review on estimation of land surface radiation and energy budgets from ground measurement, remote sensing and model simulations. IEEE Journal of Selected Topics in Applied Earth Observations and Remote Sensing 3, 225–240.

Liu, Q., Wang, L., Qu, Y., Liu, N., Liu, S., Tang, H., Liang, S., 2013. Preliminary evaluation of the long-term GLASS albedo product. International Journal of Digital Earth 6, 69–95.

Loeb, N.G., Doelling, D.R., Wang, H., Su, W., Nguyen, C., Corbett, J.G., Liang, L., Mitrescu, C., Rose, F.G., Kato, S., 2018. Clouds and the earth's radiant energy system (CERES) energy balanced and filled (EBAF) top-of-atmosphere (TOA) edition 4.0 data product. J. Clim. 31, 24.

Loeb, N.G., Kato, S., Loukachine, K., Manalo-Smith, N., 2005. Angular distribution models for top-of-atmosphere radiative flux estimation from the clouds and the earth's radiant energy system instrument on the Terra satellite. Part I: methodology. J. Atmos. Ocean. Technol. 22, 338–351.

Loeb, N.G., Loukachine, K., Manalo-Smith, N., Wielicki, B.A., Young, D.F., 2003. Angular distribution models for top-of-atmosphere radiative flux estimation from the clouds and the Earth's radiant energy system instrument on the tropical rainfall measuring mission satellite. Part II: validation. J. Appl. Meteorol. 42, 1748–1769.

Loeb, N.G., Manalo-Smith, N., Loukachine, K., Kato, S., Wielicki, B.A., 2002. A new generation of angular distribution models for top-of-atmosphere radiative flux estimation from the clouds and the Earth's Radiant Energy System (CERES) satellite instrument. In: 11th Conference on Atmospheric Radiation, pp. 9–12.

Molling, C.C., Heidinger, A.K., Straka, W.C., Wu, X., 2010. Calibrations for AVHRR channels 1 and 2: review and path towards consensus. Int. J. Remote Sens. 31, 6519–6540.

Niu, X., Pinker, R.T., 2012. Revisiting satellite radiative flux computations at the top of

the atmosphere. Int. J. Remote Sens. 33, 1383–1399.
Palle, E., Goode, P.R., Montanes-Rodriguez, P., Shumko, A., Gonzalez-Merino, B., Lombilla, C.M., Jimenez-Ibarra, F., Shumko, S., Sanroma, E., Hulist, A., Miles-Paez, P., Murgas, F., Nowak, G., Koonin, S.E., 2016. Earth's albedo variations 1998–2014 as measured from ground-based earthshine observations. Geophys. Res. Lett. 43, 4531–4538.
Pedelty, J., Devadiga, S., Masuoka, E., Brown, M., Pinzon, J., Tucker, C., Vermote, E., Prince, S., Nagol, J., Justice, C., Roy, D., Ju, J., Schaaf, C., Liu, J., Privette, J., Pinheiro, A., 2007. Generating a long-term land data record from the AVHRR and MODIS instruments. IEEE International Geoscience and Remote Sening Symposium 1021–1024.
Qu, Y., Liu, Q., Liang, S., Wang, L., Liu, N., Liu, S., 2014. Direct-estimation algorithm for mapping daily land-surface broadband albedo from MODIS data. IEEE Trans. Geosci. Remote Sens. 52, 907–919.
Riihelä, A., Manninen, T., Laine, V., Andersson, K., Kaspar, F., 2013. CLARA-SAL: a global 28 yr timeseries of Earth's black-sky surface albedo. Atmos. Chem. Phys. 13, 3743–3762.
Roca, R., Brogniez, H., Chambon, P., Chomette, O., Cloche, S., Gosset, M.E., Mahfouf, J.F., Raberanto, P., Viltard, N., 2015. The Megha-Tropiques mission: a review after three years in orbit. Front. Earth Sci. 3.
Rutan, D.A., Smith, G.L., Wong, T.M., 2014. Diurnal variations of albedo retrieved from earth radiation budget experiment measurements. J. Appl. Meteorol. Climatol. 53, 2747–2760.
Song, Z., Liang, S., Feng, L., He, T., Song, X.-P., Zhang, L., 2017. Temperature changes in three gorges reservoir area and linkage with three gorges project. J. Geophys. Res.-Atmos. 122, 4866–4879.
Stephens, G.L., Li, J., Wild, M., Clayson, C.A., Loeb, N., Kato, S., L'Ecuyer, T., Stackhouse, P.W., Lebsock, M., Andrews, T., 2012. An update on earth's energy balance in light of the latest global observations. Nat. Geosci. 5, 691–696.
Stephens, G.L., O'Brien, D., Webster, P.J., Pilewski, P., Kato, S., Li, J., 2015. The albedo of earth. Rev. Geophys. 53, 141–163.
Sütterlin, M., Schaaf, C.B., Stockli, R., Sun, Q., Husler, F., Neuhaus, C., Wunderle, S., 2015. Albedo and reflectance anisotropy retrieval from AVHRR operated onboard NOAA and MetOp satellites: algorithm performance and accuracy assessment for Europe. Remote Sens. Environ. 168, 163–176.
Suttles, J.T., Green, R.N., Minnis, P., Smith, G.L., Staylor, W.F., Wielicki, B.A., Walker, I.J., Young, D.F., Taylor, V.R., Stowe, L.L., 1988. Reflected Radiation. Vol. 1, Angular Radiation Models for the Earth Atmosphere System. NASA Reference Publication 1184.
Tang, B., Li, Z., Zhang, R., 2006. A direct method for estimating net surface shortwave radiation from MODIS data. Remote Sens. Environ. 103, 115–126.
Taylor, P.C., 2014a. Variability of monthly diurnal cycle composites of TOA radiative fluxes in the tropics. J. Atmos. Sci. 71, 754–766.
Taylor, P.C., 2014b. Variability of regional TOA flux diurnal cycle composites at the monthly time scale. J. Atmos. Sci. 71, 3484–3498.
Taylor, P.C., Loeb, N.G., 2013. Impact of sun-synchronous diurnal sampling on tropical TOA flux interannual variability and trends. J. Clim. 26, 2184–2191.
Tian, F., Fensholt, R., Verbesselt, J., Grogan, K., Horion, S., Wang, Y., 2015. Evaluating temporal consistency of long-term global NDVI datasets for trend analysis. Remote Sens. Environ. 163, 326–340.
Trenberth, K.E., Fasullo, J.T., Kiehl, J., 2009. Earth's global energy budget. Bull. Am. Meteorol. Soc. 90, 311–323.
Trenberth, K.E., Fasullo, J.T., von Schuckmann, K., Cheng, L., 2016. Insights into earth's energy imbalance from multiple sources. J. Clim. 29, 7495–7505.
Uprety, S., Cao, C., 2011. Using the dome C site to characterize AVHRR near-infrared channel for consistent radiometric calibration. Earth Observing Systems 8153.
Urbain, M., Clerbaux, N., Ipe, A., Tornow, F., Hollmann, R., Baudrez, E., Blazquez, A.V., Moreels, J., 2017a. The CM SAF TOA radiation data record using MVIRI and SEVIRI. Remote Sens. 9.
Urbain, M., Clerbaux, N., Ipe, A., Tornow, F., Hollmann, R., Fuchs, P., Werscheck, M., 2017b. Top of Atmosphere Radiation MVIRI/SEVIRI Data Record. Satellite Application Facility on Climate Monitoring.
Vermote, E., Kaufman, Y.J., 1995. Absolute calibration of Avhrr visible and near-infrared channels using ocean and cloud views. Int. J. Remote Sens. 16, 2317–2340.
Vermote, E.F., Saleous, N.Z., 2006. Calibration of NOAA16 AVHRR over a desert site using MODIS data. Remote Sens. Environ. 105, 214–220.
Von Schuckmann, K., Palmer, M.D., Trenberth, K.E., Cazenave, A., Chambers, D., Champollion, N., Hansen, J., Josey, S.A., Loeb, N., Mathieu, P.P., Meyssignac, B., Wild, M., 2016. An imperative to monitor Earth's energy imbalance. Nat. Clim. Chang. 6, 138–144.
Wang, Z., Barlage, M., Zeng, X., Dickinson, R.E., Schaaf, C.B., 2005. The solar zenith angle dependence of desert albedo. Geophys. Res. Lett. 32.
Wang, X., Key, J.R., 2005a. Arctic surface, cloud, and radiation properties based on the AVHRR polar pathfinder dataset. Part I: spatial and temporal characteristics. J. Clim. 18, 2558–2574.
Wang, X., Key, J.R., 2005b. Arctic surface, cloud, and radiation properties based on the AVHRR polar pathfinder dataset. Part II: recent trends. J. Clim. 18, 2575–2593.
Wang, D., Liang, S., 2016. Estimating high-resolution top of atmosphere albedo from moderate resolution imaging spectroradiometer data. Remote Sens. Environ. 178, 93–103.
Wang, D., Liang, S., 2017. Estimating top-of-atmosphere daily reflected shortwave radiation flux over land from MODIS data. IEEE Trans. Geosci. Remote Sens. 55, 4022–4031.
Wielicki, B.A., Barkstrom, B.R., Harrison, E.F., Lee, R.B., Smith, G.L., Cooper, J.E., 1996. Clouds and the earth's radiant energy system (CERES): an earth observing system experiment. Bull. Am. Meteorol. Soc. 77, 853–868.
Wielicki, B.A., Doelling, D.R., Young, D.F., Loeb, N.G., Garber, D.P., MacDonnell, D.G., 2008. Climate quality broadband and narrowband solar reflected radiance calibration between sensors in orbit. Proc. IEEE Int. Geosci. Remote Sens. Symp. 4.
Wild, M., 2009. Global dimming and brightening: a review. J. Geophys. Res.-Atmos. 114.
Wong, T., Wielicki, B.A., Lee, R.B., Smith, G.L., Bush, K.A., Willis, J.K., 2006. Reexamination of the observed decadal variability of the earth radiation budget using altitude-corrected ERBE/ERBS nonscanner WFOV data. J. Clim. 19, 4028–4040.
Zhang, B., Wang, Y., Hao, J., 2015. Simulating aerosol–radiation–cloud feedbacks on meteorology and air quality over eastern China under severe haze conditions in winter. Atmos. Chem. Phys. 15, 2387–2404.